From sink to source: using thermochronometric data from offshore Namibia to extract onshore erosion signals

Mark Wildman[1a*], Kerry Gallagher[1], Dave Chew[2], and Andrew Carter[3]

1. Géosciences Rennes, Université de Rennes 1, Rennes, 35000, France.
2. Department of Geology, Trinity College Dublin, College Green, Dublin 2, Ireland.
3. Department of Earth and Planetary Sciences, Birkbeck University of London, Kathleen Lonsdale Building, Gower Place, London, UK

a. Now at School of Geographical and Earth Sciences, College of Science and Engineering, University of Glasgow, Gregory Building, Glasgow, G12 8RZ, Scotland

* - Corresponding Author: Mark.Wildman@Glasgow.ac.uk

ABSTRACT

Products of onshore passive continental margin erosion are best preserved in offshore sedimentary basins. Therefore, these basins potentially hold a recoverable record of the onshore erosion history. Here, we present apatite fission track (AFT) data for 13 samples from a borehole in the southern Walvis basin, offshore Namibia. All samples show AFT central ages older or similar to their respective stratigraphic ages, while many single grain ages are older, implying none of the samples has been totally annealed post-deposition. Furthermore, large dispersion in single grain ages in some samples suggests multiple age components related to separate source regions. Using Bayesian mixture modelling we classify single grain ages from a given sample to particular age components to create 'subsamples' and then jointly invert the entire dataset to obtain a thermal history. For each sample, the post-depositional thermal history is required to be the same for all age components, but each component has an independent pre-depositional thermal history. With this approach we can resolve pre- and post-depositional thermal events and identify changes in sediment provenance in response to the syn- and post-rift tectonic evolution of Namibia and southern Africa. Apatite U-Pb and compositional data obtained during the acquisition of LA-ICP-MS FT data is also presented to help track changes in provenance and source material over time. We constrain multiple thermal events linked to the exhumation and burial history of the continental and offshore sectors of the margin over a longer timescale than has been possible using only onshore AFT thermochronological data.

Keywords: Numerical modelling, Namibian passive margin, tectonics and sedimentation, thermochronology.

Introduction

The relationship between onshore erosion and the deposition of the products in sedimentary basins ('source to sink') has been the subject of many studies over the last 20 years or so (see Helland-Hansen et al. (2016) for an overview). Due to the implicitly destructive nature of onshore erosion, most studies have focussed on the sink, or sedimentary record, either by quantifying preserved sediment volumes over time as a proxy for erosion (e.g. Leturmy et al., 2003; Rouby et al., 2009), or by using detrital geochronological/geochemical data to fingerprint source regions and constrain 'source-to-sink' lag-times (e.g. Bernet and Garver, 2005; Whitchurch et al., 2011). In geological settings that have experienced rapid and deep erosion (c. 6–12 km) (e.g. convergent mountain belts) geo- or thermochronometers with high closure temperatures such as Zircon U-Pb (>900°C) (Lee et al., 1997, Cherniak and Watson, 2001) and zircon fission track analysis (closure temperature: 240 ± 50°C) (Hurford, 1986, Bernet, 2009) are typically employed to investigate crustal formation, thermal evolution and sediment routing from the mountain range to the basin. Passive margin settings, however, tend to experience lower magnitudes of erosion, often with protracted or multi-phase erosional histories (Moore et al., 1986; Cogné et al., 2011; Ksienzyk et al., 2014; Wildman et al., 2016; Amidon et al., 2016), the details of which are not resolvable with the higher temperature systems. The Namibian sector of the southwest African 'passive' margin is a prime example of complex, multi-phase, margin evolution. Fully resolving the landscape evolution of the Namibian margin and linking this to the development of offshore sedimentary basins remains challenging.

Apatite fission track (AFT) thermochronology provides information on cooling through a relatively low temperature sensitivity range (60–120°C) and the application of this technique to outcrop samples has been used to obtain detailed information on onshore passive margin erosion histories, which have been correlated with sedimentary basin stratigraphy in passive margin settings (e.g. Gallagher and Brown, 1999; Tinker et al., 2008a). Although detrital AFT analysis has been applied in convergent settings (e.g. van der Beek et al., 2006; Homke et al., 2010; Dunn et al., 2017) its use has been limited along passive margins (e.g. Clift et al., 1996). A major obstacle to using AFT analysis on detrital apatite is introduced if the apatite has been partially annealed during post-depositional heating, typically caused by burial. If the detrital apatite is heated such that all tracks are annealed, the AFT data will only reflect post-depositional thermal events. If the detrital apatite is not annealed at all after deposition, the AFT data will hold a record of the pre-depositional history. Partial annealing will modify the AFT information in a grain during the pre-depositional phase and this effect becomes

particularly complicated if a sample is comprised of apatite holding a record of different pre-depositional thermal histories (i.e. from multiple sources). By overcoming this obstacle, we can potentially identify onshore erosion events that have been removed from the onshore AFT record.

The temporal resolution of onshore AFT is limited depending on the timing and magnitude of erosion. If a phase of erosion causes a rock to cool rapidly from temperatures hotter than the AFT closure temperature (110 ± 10°C) then the AFT data will only record this event and, potentially, subsequent lower temperature events in the thermal history. Moreover, the AFT data will not have retained information on earlier thermal events due to total track annealing (Malusà and Fitzgerald, 2019). In the context of margin evolution this means that if the total magnitude of erosion during the post-rift history was large enough (e.g. > 4 km) to cool rocks from hotter than 110 ± 10°C to the surface then these surface samples will not record syn-rift or earlier related cooling. In other words, the AFT data from single onshore surface samples can only provide thermal history information back to the time when that sample cooled below AFT closure temperature. To observe the earlier syn-rift thermal history, high temperature systems (e.g. ZFT or ZHe) may be used on the same outcrop sample, however, the thermal events that can be resolved will be dependent on initial starting temperatures of the rock prior to the onset of break-up erosion. Alternative, we propose this information can be recovered from the detrital AFT record.

Here, we present an AFT dataset from a borehole, offshore of Namibia in the south Atlantic (Fig. 1). As a consequence of low burial-related maximum temperatures, the samples have preserved a record of their onshore provenance, or pre-depositional, thermal history. Despite considerable dispersion in the single grain age data, we show that some of this signal can be extracted, as well as the post-depositional thermal history. The results imply that the offshore sediments record rapid erosion at the time of rifting, a signal not obvious in the AFT data from onshore surface samples. As detailed below, the AFT dataset combines single grain ages collected using the long-established external detector method (EDM) and ages collected using the novel LA-ICP-MS method and provides an opportunity to directly assess the comparability of the two approaches.

Geological setting

The basement in Namibia comprises Palaeoproterozoic and Meso- to Neoproterozoic gneisses and supracrustal rocks (Kroner et al., 2004) (Fig. 1a). On top of the basement are the

siliciclastic-carbonate successions of the Damara Supergroup, which experienced high P-low T metamorphism along the southern branch of the intracontinental Damara metamorphic belt during Pan-African (600–480 Ma) orogenesis (Miller, 1979). The central Damara orogen experienced low P–high T contact metamorphism associated with the emplacement of voluminous granitic plutons at 540–500 Ma (Jung et al., 2019, 2020).

The tectonic structure of the Damara Orogen is characterised by NNW trending transpressional faults of the northern Kaoka and southern Gariep Belts and the ENE trending structures in the main central Damara Belt formed during convergence between the Congo and Kalahari cratons (Passchier et al. 2002; Frimmel, 1995; Miller, 1983). Major NE-SW trending tectonic lineaments define the regional structural trend in the Damara Belt. These are believed to reflect major, reactivated NE-SW trending structures within the pre-Damara metamorphic basement that controlled the location of Damara Supergroup sedimentation in rift basins (Tankard et al., 1982). The Pre-Cambrian tectonic framework in Namibia, as elsewhere in Africa, has had a major influence on Phanerozoic tectonic events (Clemson et al., 1997; Holzförster et al., 1999; Raab et al., 2002; Salazar-Mora et al., 2018; Will and Frimmel, 2018).

The Permo-Triassic sedimentary rocks of the Karoo Supergroup, which cover much of the southern African interior, are only present in sporadic fault-bounded outliers in Namibia (Fig. 1a). Jurassic–Early Cretaceous clastic sediments were sourced from the local basement and were likely deposited in syn-rift fault-bounded basins. The Early Cretaceous Etendeka flood basalts cover these sediments (Fig. 1a) and have been dated at 134–127 Ma, which is coeval with the Parana flood basalts in NE Brazil (e.g. Gibson et al., 2006). This large igneous province is attributed to magmatic processes associated with West Gondwana passing over the Tristan da Cuhna hotspot (O'Connor et al., 2012; Hoernle et al., 2015), contemporaneous with the northward-propagating breakup of South America from Africa. The onshore post-rift geology is limited to minor alkaline intrusions and thin (0–400 m) terrestrial Cenozoic deposits of the Kalahari Group that thicken toward the northeast (Ward, 1988; Ward and Martin, 1987; Marsh, 2010; Wanke and Wanke, 2007).

Onshore, the present-day Namibian margin topography is dominated by a broadly coast-parallel escarpment zone lying c. 80–100 km inland from the present-day coastline (Fig. 1b). The escarpment marks the transition from a low-lying, low-relief coastal zone to an elevated (c. >1 km), low-relief interior plateau. The coastal escarpment varies along its length becoming more prominent and characterised by a higher relief in places, while in others it diminishes and

is harder to define from the increasing elevation of the gently convex-up coastal zone. The elevated plateau is a dominant and enigmatic feature that spans the continental interior of southern Africa. Immediately inland of the escarpment the plateau has a concave-up sloping profile with decreasing elevation over c. 100–200 km. The Swakop river valley follows the structural trend (ENE) of the Okahanja Lineament and Damara Metamorphic Belt (Fig. 1b) and bounds the region of highest elevations to the North. Sporadic inselbergs linked to Early Cretaceous alkaline intrusions (e.g. Brandberg) form local points of high elevation along the margin (Fig. 1b).

Offshore, the stratigraphy preserved in the Walvis and Orange Basins are a direct product of geological processes and the delivery of sediments during erosion that formed the topography of southwestern Africa (Fig. 1c). Borehole 2213/6-1 was drilled into the Koigab Fault zone in the Walvis Basin (Clemson et al., 1997), which is a structural high relative to the main Walvis Basin to the west. The Koigab Fault Zone is part of the Namib Rift, which commenced in the Carboniferous-Permian, and was an extensional fault system until inversion and erosion during the mid-Triassic. The well log of the borehole shows interbedded sequences of claystone and fine- to coarse-grained sandstone overlying layered units of continental volcanic rocks and siliciclastic sediments likely related to the emplacement of Etendeka lavas and onshore erosion during the syn-rift phase, respectively, and comparable to the wedges of interlayered basalts and aeolian sands observed at the Kudu gas field in southern offshore Namibia (de Vera et al., 2010).

The general stratigraphy of the Walvis Basin is summarised in Fig. 1c and discussed in greater detail by Holtar and Fosberg (2000) and Baby et al. (2018). Post-rift successions overly a rifted continental basement with Late Jurassic to Early Cretaceous siliciclastic and volcanic rocks deposited in N-S trending syn-rift grabens (Clemson, 1997; Clemson et al., 1999, Light et al., 1993). The stratigraphy of the mid-Late Cretaceous and Cenozoic post-rift sequences in the Walvis Basin is dominated by siltstones, claystones and minor sandstone interbeds that were deposited in in marine shelf, slope and basin environmental settings and which imply significant post-rift erosion has occurred (Clemson et al., 1997; Holtar and Fosberg, 2000; Baby et al. 2018). The Late Cretaceous succession also exhibit large-scale gravity driven fault structures, which are associated with episodic gravitational collapse driven by uplift of the onshore domain in the Late Cretaceous (de Vera et al., 2010). The boundary between the syn-rift and post-rift sequences is the Late Hauterivian (132.9 ± 2 to 129.4 ± 1.5 Ma) breakup unconformity (Light et al., 1993; Baby et al., 2018). Additional unconformities are observed

in the lower Campanian (c. 81 Ma), top Maastrichtian (c. 66 Ma), middle Oligocene (c. 30 Ma) and upper Miocene (c. 11 Ma) (Fig. 1c) (Baby et al., 2018).

During the Early Cretaceous (c. 130–113 Ma) initial post-rift phase, the Walvis Basin accumulated an estimated 1.04×10^4 km of sediment (Baby et al., 2020). The largest volumes of sediment were deposited during the mid-Late Cretaceous (23.15×10^4 km) (Baby et al., 2018) with c. 3 km of sediment deposited in the vicinity of the borehole location over this time (Baby et al., 2020). Cenozoic sediment volumes are estimated to be 8.79×10^4 km with a thickness of up to c. 1800 m in the main depocenter of the basin and c. 600 m in the vicinity of the borehole (Baby et al., 2018).

Apatite Fission Track Thermochronology

Methods

Apatite fission-track data were obtained from 13 samples from cuttings, over a depth range of 650–2555 m, from borehole 2213/6-1 (Fig. 1). The AFT data we present here are a composite dataset comprised of currently unpublished data collected in the 1990s (dataset referred to as AFT-90, SI-Table 1) and new LA-ICP-MS AFT data collected for this study (SI-Table 2). The new data were collected on the same grain mounts as the AFT-90 dataset although not necessarily on the same grains.

The AFT-90 age data were acquired using EDM (Hurford and Green, 1983) and 20–21 grains were dated for all samples. The dataset includes horizontal confined track (CT) lengths and c-axis angles but no composition or proxy (Dpar) measurements. These data were used to demonstrate multi-sample inverse thermal history modelling by Gallagher (2012) (see Fig. 10 in Gallagher, 2012).

New AFT age data were acquired using the LA-ICP-MS protocol described by Chew et al. (2012) and Cogné et al. (2020) (SI-Table 3). Fission tracks were counted using a Zeiss AxioImager M1m microscope and Autoscan Fission Track Studio software. Additional horizontal and inclined (corrected for dip angle in Fission Track Studio) CTs were also measured, but only in grains that were counted so that track lengths can be directly associated with an AFT age. Five Dpar measurements were made on each counted grain as a proxy for compositional influence on annealing for each counted grain. Chlorine content was also measured on each analysed grain following the protocol described by Chew et al. (2014a) as well as additional compositional data for which a subset of elements (e.g. Sr, Y, LREEs [La,

Ce, Pr and Nd]) is presented in SI-Table 3. For each grain ablated for FT analysis, we obtained an apatite U-Pb age (e.g. Cogne et al., 2020; Chew et al., 2014b) and we also obtained additional U-Pb on randomly selected apatite grains in several of the borehole samples (SI-Table 3).

The AFT-90 data and new LA-ICP-MS AFT data have similar AFT ages and track length data (Fig. 2a, c). The age difference between the AFT-90 and LA-ICP-MS dataset is 0.60–1.00 and although the specific value of the AFT-90 central ages are younger than the LA-ICP-MS AFT central ages, nine out of the 13 samples overlap within uncertainty of the 1 to 1 relationship line. The range in age difference does not correlate with the central AFT age or composition (Fig. 3). There does seem to be some correlation with the largest age differences and the single grain age dispersion particularly for the AFT-90 dataset (Fig. 2b). The amount of single grain age dispersion is similar for the AFT-90 and LA-ICP-MS age dataset with average dispersion of 35% and 40% respectively. In some cases, the LA-ICP-MS AFT dataset lowers the amount of age dispersion (e.g. MT2353) and in others it increases the age dispersion (e.g. MT2355). This can be interrogated further using the radial plot (Fig. 3) or the classical χ^2 statistic(see SI-Table 1 and SI-Table 2). It is apparent that the initial number of grains counted in the AFT-90 study were generally insufficient to characterise the amount of single grain age dispersion in the samples. Moreover, the difference between the EDM and LA-ICP-MS age seems to broaden in samples with greater age dispersion, which may be attributed to the relative precision associated with measuring U content by counting induced tracks with the EDM method versus measuring U directly via laser ablation. AFT ages collected using EDM and LA-ICP-MS AFT approaches are generally considered to be consistent (*cf.* Seiler et al., 2014, Cogné et al., 2020), however more comparison datasets are required to better support this assumption. Given this assumption, we present all the age data as a single dataset (Table 1). We did not include track lengths measured in the original AFT-90 analysis because they do not have an associated measured grain age.

To facilitate the integration, plotting, and modelling of the EDM age data with the LA-ICP-MS age data, we determine an equivalent value for the number of induced tracks (N_i) for each grain dated using LA-ICP-MS based on the measured LA-ICP-MS AFT age and its uncertainty and employing the zeta calibration factor, ρ_d and N_d (track density and number of tracks counted for the U dosimeter) from the AFT-90 EDM analyses.

227 ***Results***

228 The combined data set shows central AFT ages from 90.2 ± 3.5 to 317 ± 33 Ma (Table 1). All
229 samples fail the χ^2 test at the 5% level and have large dispersion (23–82%). Mean track lengths
230 (MTLs) range from 10.45 ± 0.18 to 12.70 ± 0.11 μm and decrease with depth, a trend that is
231 consistent with some partial annealing post-deposition (Table 1). Track length distributions
232 (TLDs) are unimodal and generally fairly broad and normally distributed. Some TLDs show
233 slight tails of short (< 12 μm) tracks (see SI-1 for TLDs).

234 The dispersion of single grain ages and the presence of multiple age populations is more
235 pronounced in radial plots (Fig. 3) for some samples (e.g. MT2352) more than others (e.g.
236 MT2357). The compositional proxy, Dpar, available for the new data only, generally does not
237 show any clear relationship with the AFT ages, suggesting that composition is not the dominant
238 control on the dispersion. For MT2352, while it is clear that the older component has larger
239 Dpar, the large disparity in ages and present day shallow crustal (i.e. low temperature) position
240 of the sample, it is plausible that the dispersion represents distinct pre-deposition erosion
241 histories leading to a mixture of age populations. Our measured Cl wt% values are generally
242 positively correlated with Dpar (see SI-2) and although this is likely to be the dominant
243 compositional influence on fission track annealing (Barbarand et al., 2003) we use Dpar in the
244 modelling as a proxy to constrain the bulk compositional influence on track annealing.

245 Pan-African (c. 600–500 Ma) apatite U-Pb ages are dominant in every sample. Deeper than -
246 1410 m (i.e. samples MT2354 to MT2363) almost all ages are Pan-African with only
247 occasional grains showing older Proterozoic ages or younger Permo-Triassic (i.e. Karoo) ages.
248 Shallower than -1410 m (i.e. MT2353 to MT2351), there is a greater diversity of ages, with the
249 clear Pan-African signal mixed with a larger abundance of Meso- to Neoproterozoic (c. 1.5–
250 0.8 Ga) ages and, particularly for MT2352, a significant number of Palaeoproterozoic to
251 Archean (i.e. >2 Ga) ages (see SI-Table 3).

252 Following the approach of O'Sullivan et al. (2020) we plot the data on a Sr/Y vs. ΣLREE biplot
253 to determine the general source lithology of detrital apatite (Fig. 4a). The majority of the grains
254 can be traced to high-grade metamorphic rocks and some low to medium metamorphic rocks
255 (Fig. 4b, c). A small cluster of points are observed in the top right of the plot suggest a source
256 comprising of ultramafic rocks and alkaline-rich igneous rocks. This cluster clearly corelates
257 with the oldest AFT ages and apatite U-Pb ages (Fig. 4b, c).

Given the comments above, we assume that the dispersion in all samples reflects a mixture of different provenance related or pre-depositional thermal history signals. Carter and Gallagher (2004) showed provenance information can be obtained from samples that have undergone post-depositional annealing, especially where the pre-deposition history involved protracted cooling as indicated by the presence of Palaeozoic AFT ages in our samples. In an attempt to extract these signals, we first use AFT mixture modelling to identify discrete age components for each sample. Then we assign each measured single grain age to the most probable age component to define 'subsamples' to be used for inverse thermal history modelling. These subsamples also incorporate any track length data associated with the assigned single grain ages.

Mixture modelling

The transdimensional Bayesian mixture modelling approach presented by Jasra et al. (2006) is used to identify the number of age components in each sample. In this approach, we obtain a probability distribution on the number of components. This avoids needing to specify in advance the number of components, and instead we choose the most probable number of components. We can also classify each of the measured single grain AFT ages into a given age component based on the probability of a given grain coming from a particular age component. We note that annealing can lead to dispersion in ages such that an initially symmetrical single component age distribution may become asymmetrical and then a skew distribution model is more appropriate than a symmetrical (e.g. Gaussian) component distribution that may lead to an overestimation of the number of components. Therefore, we assume skew-t distributions for the form of the component age distributions. A skew-t distribution (see Jasra et al, 2006) is defined by the location and scale parameters (similar to the mean and standard deviation) with two additional parameters defining the left and right skewness. The Gaussian distribution is a special case of the skew-t distribution for which the two skewness parameters are equal and large. The final parameter is the proportion of an age component contributing to the overall combined distribution. Given the parsimonious nature of Bayesian inference, the approach we adopt also tends to prefer less rather than more components. However, inferring too many age components may not present a problem as we would expect the thermal histories to be similar, for example, if two inferred components really come from just one.

We ran 1-2x10^6 iterations of the Markov chain Monte Carlo sampler. As explained in more detail by Jasra et al. (2006 and references therein), the inference of age components is based

on modelling the unknown, 'true' ages, rather than the measured ages (which have measurement uncertainty). In practice, this means for each measured age, we resample an age from a Gaussian distribution with a mean equal to the measured age and a standard deviation equal to the measurement uncertainty. The set of resampled ages are then used for the inference of age components at each iteration. At the end of the sampling iterations, we choose the maximum of the posterior probability distribution on the number of components (Fig. 5). Given this maximum posterior estimate, we construct a predicted distribution for each age component, weighted by the estimated proportion, using the expected values for the mean and standard deviation. From these, we can choose the age component distribution that yields the maximum probability for a measured single grain age from both the AFT-90 and LA-ICP-MS data sets and allocate the measured single grain age to that component (Fig. 5).

We did not include track lengths measured in the original AFT-90 analysis because they do not have an associated measured grain age. However, all track lengths and Dpar values from the new LA-ICP-MS dataset were measured on grains that were also dated, so we can also assign length and Dpar measurements to a specific age component for each sample. Therefore, for any sample with multiple components, we create 'subsamples' that have a track length distribution, a distribution of Dpar values, defined by a mean and standard deviation, and single grain ages assigned to a discrete component (based on both the AFT-90 and LA-ICP-MS age data) (Fig. 6, SI-Table 4).

THERMAL HISTORY MODELLING

Model set-up

Thermal history modelling was performed using a Bayesian multi-sample vertical profile inversion approach (Gallagher, 2012). The methodology behind this approach has been described in detail in Gallagher et al. (2005) and Gallagher (2012) but, to summarise, we take a suite of samples at different depths (as in our borehole dataset) and look for a general thermal history, including palaeotemperature gradients, that can adequately predict the data for all samples.

All samples are terrigenous siliciclastic sediments composed of material transported from the onshore Namibian continental margin. Due to a paucity of fossil material, their stratigraphic ages are not well defined (Fig. 7, Table 1). Consequently, each sample is assigned a loose stratigraphic time-temperature constraint, sampled from uniform distributions for a range in

the time of deposition and a temperature of 10 ± 10°C. During the inversion runs, the stratigraphic age for each sample is drawn from these prior distributions. Present-day temperature constraints were estimated from downhole temperature (corrected BHT) data. These are consistent with a geothermal gradient of 25 ± 5°C/km and a surface temperature of around 4°C. The palaeo-temperature gradient was assumed to be constant over time, but the actual value was allowed to vary between 25 ± 10°C/km. No other constraints, such as possible episodes of erosion inferred from unconformities observed in the main depocenters of the basin (e.g. Fig. 1c), are imposed on the model. Instead we let the data decide when episodes of heating and cooling are required and discuss the implications of these thermal events below alongside observations from the offshore stratigraphy.

As described above, we combined the old and new AFT age data for each sample, used mixture modelling to identify age components, classified each single grain age to a given age component and extracted the track length measurements and Dpar values associated to those single grain ages (from the new AFT data) to form a subsample. For thermal history modelling, we adopted the multi-compositional fission-track annealing model of Ketcham et al. (2007). We allowed Dpar to vary during the inversion runs, resampling values from a normal distribution, with the mean and standard deviation equal to the mean and standard deviation of all Dpar measurements for each subsample. Letting the compositional proxy vary in this way provides some flexibility in the modelling to allow for the dispersion in the measured Dpar values, and the fact that the annealing models have inherent uncertainty in their construction and calibration.

All subsamples from a given sample were required to have the same post-depositional thermal history. However, we allowed each subsample to have an independent pre-depositional thermal history. To simulate the pre-depositional thermal history, we included an additional independent time-temperature (t-T) point for each subsample, which is required to be before the time of the stratigraphic age constraint. In this way, the pre-depositional thermal history is parameterised as linear cooling from an unknown t-T point (a distribution of which is estimated during the inversion) to the stratigraphic age temperature constraint. This is the simplest parameterisation for the pre-depositional thermal history and will effectively constrain the average rate of cooling over the inferred duration prior to deposition. The fission track age, MTL and TLD predicted by the model is a product fission track annealing over the pre- and post-depositional portion of the thermal history. The distribution of time-temperature points

forming the initial part of the pre-depositional thermal histories can be visualised in 2D plots in SI-3, and in these we often see a trade-off between time and temperature.

Inverse modelling results

The expected thermal history model for the borehole, post-200 Ma (see SI-4 for longer thermal history), is shown in figure 7a, and the summary predictions for this model are given in figure 7b. The overall trends of the measured AFT and MTL subsample data with depth are well reproduced by the modelled data.. The maximum post-depositional temperatures are < 110°C for the deepest sample and < 60°C for the shallowest sample. This implies that fission tracks in most, if not all, of the samples have not been totally annealed post-deposition. In other words, the data are potentially providing information about erosion-related cooling prior to deposition, albeit in a relatively simple way, given the nature of the parameterisation we adopted.

Pre-depositional thermal histories

The pre-depositional components of the thermal history can be classified into three groups (Table 2) (SI-4). Nine subsamples, (Group I) all with relatively old single grain AFT ages, show protracted cooling initiated prior to 150 Ma (Fig. 7a) (see SI-4 for the thermal history beyond 200 Ma). Eleven subsamples (Group II) show rapid cooling across the base of the Partial Annealing Zone (PAZ) between 145–125 Ma (Fig. 7a). The three shallowest samples (Group III) show rapid cooling in the Late Cretaceous. Two subsamples show rapid cooling initiating at between 100 and 90 Ma and one shows rapid cooling starting at 70 Ma (Fig. 7a). Occasionally pre-depositional thermal history paths can be seen to start in the middle of the PAZ. In these cases, it is implicit that the samples cooled rapidly from temperatures hotter than the bottom of the PAZ just prior to this time.

Using each sampled thermal history, we also make a prediction for the AFT closure time (t_c) for each sample component. As track formation occurs at a more or less constant rate over the duration of a thermal history, each track has an effective formation age. In modelling track annealing over time, we follow the approach described by Crowley (1993) in which the thermal history, divided into isothermal time steps of around 1 m.yr., is run backwards in time. This allows us to easily monitor the time when the oldest simulated track is totally annealed, and by implication, all tracks present at that time would also have been totally annealed. We refer to this time as the closure time, t_c, and there will be a corresponding temperature at that time in the thermal history, which could be considered as the effective closure temperature. The AFT

384 t_c is then a model calculation and will be older or equal to the measured AFT age. It can be
385 taken as an indication of the maximum time to which the thermal history can be resolved. It
386 will reflect compositional controls on annealing as these will change the effective closure
387 temperature of the sample. During the inversion iterations, both the thermal history and Dpar
388 can vary, and so we obtain a distribution of AFT t_c that incorporates these variations. We use
389 the average and standard deviation of this distribution as an estimate and uncertainty of AFT t_c
390 for each subsample (Fig. 8).

391 Taking all estimates of AFT t_c for each subsample shows that the dominant population is Early
392 Cretaceous (syn-rift, c. 145–125 Ma) with a smaller population in the Triassic-Carboniferous
393 (c. 320–240 Ma) and some sample components making up a mid-late Cretaceous (post-rift,
394 110–80 Ma), a Cambrian-Proterozoic (Pan-Africa, c. 560–500 Ma) and a Neoproterozoic (c.
395 820–760 Ma) population (Fig. 8). In terms of the downhole trends, the deepest
396 (stratigraphically oldest) sample yields a late Palaeozoic-early Mesozoic t_c (223±25 Ma)
397 indicating that, prior to syn-rift erosion, the rocks containing apatite were already at relatively
398 low temperatures (Fig. 7a, Fig. 8) onshore. With subsequent deposition of more syn-rift
399 sediment, an onshore rift-related rapid cooling signal becomes more dominant (Fig. 7a, Fig. 8).
400 The predicted AFT t_c for the sample components from 2460 m (MT2362) to 1410 m (MT2354)
401 depth are around 147 ± 9 to 123 ± 1 Ma, although some of these samples still contain a
402 population of grains with an older (>200 Ma) t_c (Fig. 8). In the shallower samples, e.g. 1120 m
403 (MT2353), this syn-rift signal is no longer apparent but there is a mid-Cretaceous AFT t_c (Fig.
404 8) caused by rapid pre-depositional cooling at this time (Fig. 7a). This signature is present at
405 870 m (MT2352), but this sample also apparently records slow cooling since the Proterozoic
406 before deposition in the Late Cretaceous (Fig. 7a). The shallowest sample at 650 m (MT2351)
407 also shows a mixed AFT t_c signal (Fig. 8), reflecting the cooling episodes already observed
408 over the Proterozoic and Early Cretaceous as well as a younger Late Cretaceous AFT t_c (Fig.
409 8) and associated pre-depositional rapid cooling signal (Fig. 7a).

410 *Post-depositional thermal history*

411 The inferred post-depositional thermal history of the borehole profile can be characterised by
412 several stages (Fig. 7a). (i) From approximately 120 Ma, there is a variable rate of heating,
413 initially relatively slow, then c. 90–65 Ma, there was phase of accelerated heating bringing the
414 deepest sample from temperatures of 32–48°C to between 92 and 106°C, the maximum
415 palaeotemperatures. Over most of post-depositional thermal history, the geothermal gradient is

inferred to be c. 20°C/km but varies occasionally to 25°C/km (e.g. at 80 Ma) and ends at 25°C/km, consistent with the present day measured geothermal gradient as imposed in the prior. Given the range of predicted geothermal gradients, the upper and lower limits of temperature change from 90–65 Ma and an assumption of steady state heat transfer, the amount of heating equates to burial under c. 1.8–3.7 km of sediment, or a heating rate of ~1.5–2.0°C/m.y. Coincident with the onset of this mid-Late Cretaceous burial-related heating, is rapid pre-depositional cooling associated with the shallowest samples (clearly yet to be deposited), implying a link between increase in the rates of onshore erosion and offshore deposition at c. 90 Ma. (ii) Following the period of burial related heating, there is a period of rapid cooling around 8–9°C/m.y. in the basin at the end Late Cretaceous/Early Cenozoic (40–45°C during 65–60 Ma), equivalent to around at least 1.6–2.3 km of eroded section. The sediments equivalent to the two youngest/shallowest samples were subsequently deposited in the basin but, in comparison to the deeper samples, their pre-depositional thermal histories reflect older cooling events. (iii) From 60–35 Ma, the entire profile is heated by c. 30°C, or around 1°C/m.y., equivalent to c. 1.2–1.5 km of overburden. (iv) The final thermal event is a period of cooling of around 20°C to bring the samples to their present-day temperatures. This could imply around 0.8–1 km of erosion, but as we discuss below, this inferred cooling may reflect other controls.

DISCUSSION

The inferred thermal history combined with the estimates of AFT t_c for each sample age component reveals information on both onshore and offshore thermal events. These events are now considered alongside the additional apatite U-Pb and compositional data we obtained, the existing onshore thermochronology data and observations on the timing and magnitude of offshore sedimentation to show that thermochronology data from sedimentary basins can reveal information on the sediment source region thermal history. Zircon fission-track, AFT and Apatite (U-Th)/He data in the onshore region adjacent to the borehole (c.f. Fig. 1b) are shown in SI-5. The regional thermochronology dataset for Namibia and southern Africa is shown and discussed in detail in Wildman et al. (2019) and Krob et al. (2020).

Most of the samples in the borehole were deposited during the Early Cretaceous (c. 120±20 Ma), which overlaps with the syn-rift phase (145–125 Ma) and the beginning of the first post-rift event in the mid- to Late Creatceous (post-rift (i): 110–80 Ma). The AFT age components revealed from mixture modelling, the t-T paths predicted by the thermal history model and the

estimates of AFT t_c all suggest that samples deposited during the syn-rift period contain a mixture of apatites that (i) cooled slowly and resided at temperatures <60°C pre-rift, or (ii) cooled rapidly due to enhanced rift-related erosion. The shift from a greater proportion of pre-rift cooling closure ages at greater depth (e.g. from 2555 m [MT2363] to 2230 m [MT2359]) to a dominance of syn-rift closure times in shallower samples (e.g. 2100 [MT2358] to 1410 m [MT2354]) (Fig. 8) is consistent with continuous onshore erosion of the pre-rift surface that first removes rocks residing above or in colder parts of the PAZ, and so have older AFT ages (Fig. 9a). These erosion products were then transported and deposited in the basin. With the onset of rifting, enhanced erosion exhumes material deeper in or hotter than the PAZ. This rapid cooling yielded apatites with syn-rift AFT ages that were deposited in syn-rift sediments on top of the earlier sediments with older pre-rift AFT ages in the offshore basin (Fig. 9b, c). Rapid denudation at the time of rifting has been advocated along several passive margin settings driven by erosion in response to rapid base-level fall and/or regional or local tectonic uplift (Gilchrist and Summerfield, 1990; van der Beek et al, 2002). Onshore AFT data along African margins and other passive margins globally have been interpreted in terms of a rift-related increase in erosion rate (e.g. Wildman et al., 2015, 2016, Gallagher et al, 1998, Gallagher and Brown 1997, 1999) (Fig. 10).

Apatite U-Pb ages from samples MT2354 to MT2363 (i.e. > -1410 m), are predominantly in the range 650–450 Ma (i.e. Pan-African), with a median value of 528 Ma, and mean of 597 Ma. Several grains from MT2359, show older, Neoproterozoic (c. 0.8–1 Ga) apatite U-Pb ages, however in the other samples only sporadic grains yield ages that are Neoproterozoic or older. Similarly, occasional grains, show younger ages contemporaneous with the deposition of the Karoo Supergroup (i.e. Permian – Triassic). Regardless of the measured apatite U-Pb age or the AFT age component to which single apatite grains belong to, the majority of grains plot in the high-grade metamorphic rock field on the Sr/Y *vs* ∑LREE bivariate plot (Fig. 4d).

As discussed below, in the Namibian Damara Belt (Fig. 1a), the magnitude of post-rift erosion has been large enough to remove any obvious record of the syn-rift event in AFT data from single surface bedrock samples. However, recent modelling of a vertical profile of AFT and apatite (U-Th)/He data from the Brandberg Massif, has shown cooling between 130–100 Ma (Margirier et al., 2019). Further north along the Kaoko Belt, Krob et al. (2020) present zircon fission-track data that yield ages of 310 to 430 Ma. AFT ages presented by Krob et al. (2020) range from c. 60–390 Ma, but many AFT ages are Early to middle-Cretaceous and are attributed to thermal resetting during the emplacement of the Etendeka volcanics followed by

protracted cooling. In addition to heating from the volcanics these rocks may have been reset due to their depth in the crust and initially resided below the section that recorded rapid syn-rift cooling, which was eroded and deposited in the offshore (Fig. 7). Erosion at this time is also supported by sediment volume estimates in the Orange and Walvis basins that suggest an influx of sediment at the time of rifting (e.g. Rouby et al., 2009; Guillocheau et al., 2012; Baby et al., 2020) (Fig. 10).

Following syn-rift erosion and sedimentation, the inferred thermal history implies relative stability until c. 90 Ma consistent with a reduction in tectonic activity following continental break-up (Fig. 7a). Estimates of sediment accumulation rates in offshore basins varies, with the southern Orange Basin having higher sedimentation accumulation rates than the Walvis Basin in the north (Guillocheau et al., 2012). However, more recent work on sediment volumes in the Walvis Basin by Baby et al. (2020) has predicted accumulated volumes remained relatively high during the mid-Cretaceous (Fig. 10). It is possible that the borehole location did not experience burial-related heating during this time because (i) there was a coincident decrease in heat flow, (ii) the total amount of sediment deposited was too low to cause a recordable thermal effect or (iii) the sediment bypassed the borehole and was deposited in more distal parts of the margin.

At 90 Ma, the data imply a period of rapid post-depositional heating, considered most likely to be burial related (Fig. 9d). The timing of this agrees with the well-documented onshore mid-Cretaceous cooling episode (c. 110–80 Ma) inferred from AFT and AHe data from along the southwest (Kounov et al., 2009; Wildman et al., 2015, 2016), southern (Tinker al., 2008b; Green et al., 2016) and southeast (Brown et al., 2002) margins of southern Africa and across a large section of the southwestern African plateau (Wildman et al., 2017; Stanley et al., 2013; Kounov et al., 2013) (Fig. 10). The thermal histories for subsamples from 1120m and 870m depth show rapid pre-depositional cooling just prior to deposition and yield t_c estimates of 101±3 Ma and 95±1 Ma, respectively (Fig. 8). The onshore mid-Cretaceous cooling event has been interpreted as a result of regional denudation and is supported by increased sedimentation rates and volumes in the offshore Namibian and South African basins (Guillocheau et al., 2012; Tinker et al., 2008a; Baby et al., 2020; Rouby et al., 2009) (Fig. 10).

Regional uplift and westward tilting caused by the African plate moving over a buoyant mantle superplume has been suggested as a mechanism to explain the pattern and timing of onshore erosion and offshore accumulation (Fig. 10) in the mid- to Late Cretaceous (c. 100–65 Ma)

(Braun et al., 2014). However, spatial variations in apatite thermochronology data and thermal histories across structural lineaments along the margin and at the interior craton boundary suggests local structural controls are also important (Raab et al 2002; Kounov et al., 2009; Wildman et al. 2015, 2016, 2017). Despite the mid- to Late Cretaceous (c. 110–80 Ma) being the predominant cooling signature onshore, it is largely absent from our thermal history, except for two sub-samples showing pre-depositional cooling at this time. The limited record in the borehole samples of pre-depositional cooling corresponding to the first post-rift event in the mid- to Late Cretaceous ('post-rift (i)') (110–80 Ma) may be a consequence of later erosion, observed in the thermal history as rapid cooling at 65–60 Ma (Fig. 7a), which removed the mid- to Late Cretaceous sediments that contained this record (Fig. 9e). Additionally, subsidence of the distal margin and uplift of the proximal part of the offshore region in the mid-Cretaceous (de Vera et al., 2010) may have resulted in most of the sediments delivered to the Atlantic at that time accumulating further oceanward than the location of the borehole.

The most significant post-depositional cooling episode occurs at c. 65–60 Ma. This timing is dominant in the onshore cooling signal across the Damara Belt in north-western Namibia adjacent to the basin where our borehole is located (Raab et al., 2002, 2005; Brown et al., 2014). Many of the measured AFT ages onshore are in the range 60 to120 Ma, with Late Cretaceous AFT ages forming a clear spatial relationship that matches the NE-SW trend on the Damara Belt and extends c. 400 km inland on to the interior plateau (Fig. 2 in Raab et al., 2002). The surrounding AFT ages are older than the timing of rifting and are commonly >300 Ma. Thermal modelling of the AFT data implies rapid cooling began between 80–60 Ma in the Damara Belt and this has been attributed to a post-rift event ('post-rift (ii)') involving local reactivation of NE-SW shear zones (Fig. 1) in response to a change in plate motions (Raab et al., 2002; Brown et al., 2014). Geophysical data show that the major Pan-African tectonic lineaments of the Damara Orogen extend well into the offshore domain (Corner, 2000) and may have also experienced local reactivation accompanied by denudation. A provenance signal with a record of onshore cooling at this time is only observed for one age component in the shallowest sample, deposited just after this cooling episode (Fig. 7a). This sample has two other age components with older estimated AFT t_c values (130 Ma and 280 Ma) (Fig. 8). This suggests that, apart from areas of local reactivation, the magnitude of onshore erosion was generally not enough to exhume and remove rocks from depths in the crust that were hot enough (in or hotter than the PAZ) to have registered this Late Cretaceous cooling event.

The two shallowest samples (MT2351 and MT2352) have age components with Late Palaeozoic, Early Palaeozoic and Neoproterozoic t_c, respectively (Fig. 8). These timings are consistent with the onshore AFT record observed inland of the escarpment and to the north and south of the Damara Belt where measured AFT ages are >300 Ma. The presence of this signal offshore could reflect a change to the drainage patterns, driven by structural reactivation and fault block uplift that pushed erosion further inland than the escarpment, or by simply allowing erosion products from further inland, with older AFT ages, to reach the offshore basin (Fig. 9e).

The change in provenance signal shown in the AFT data and in the pre-depositional thermal history paths for the shallow samples (MT2351–MT2353) is reflected in a change in the pattern of apatite U-Pb ages. In these samples, there is a greater amount of grains with Neoproterozoic U-Pb apatite ages. A significant proportion of ages, particularly for MT2352, are Archean in age, which supports our interpretation that onshore post-rift erosion moved inland and exhumed the previously slowing eroding interior cratonic regions due to regional uplift and/or movement along the faults along the Damara orogenic belt. Further support of this interpretation is provided by the Sr/Y *vs* ∑LREE bivariate plot for MT2352 (Fig. 4e). This shows a significant cluster of datapoints straddling the ultramafic/alkali-rich igneous fields of the plot, which correspond to the older single grain AFT and U-Pb ages in MT2352 (Fig. 4b). The shallowest sample, MT2351, shows a far more mixed apatite composition that does not correlate with the AFT age component to which the apatites are assigned (Fig. 4f), and an absence of Archean U-Pb ages. This may indicate another change to the source region from the interior craton to the younger (i.e. Neoproterozoic) basement and Pan-African rocks that still outcrop onshore.

A late Eocene-Early Oligocene (c. 35–30 Ma) surface uplift event has been proposed based on regional mapping of geomorphic planation surfaces, river profile analysis, and the identification of a regional offshore erosional unconformity at this time. Planation surfaces are typically low-relief, weathered surfaces covering various elevations. Recent work has revised the identification and classification of African planation surfaces and other geomorphic features (see Guillocheau et al., 2018; Dauteuil et al., 2015; Picart et al., 2020). The prevailing climate conditions over a time period drives the erosion and/or weathering process that formed a particular landform, while tectonic processes affect the geometry of the surfaces. Quantitative dating of the formation and deformation of planar weathered surfaces remains challenging (e.g. Vasconcelos and Carmo, 2018) and more commonly dating relies on ascribing relative age ranges based on the vertical position and geometries of different surfaces and their relationships

to any available well-dated geological markers (e.g. Picart et al, 2020). Based on the geometries of the surfaces Picart et al. (2020) conclude that a long-wavelength bulging occurred during the Oligocene. This bulging is suggested to be a consequence of spreading rate changes at the end of the Eocene. Surface uplift in the Oligocene is suggested to be on the order of 400–500 m and has also been attributed to sea-level fall and small-scale convection in the upper mantle causing tilting of the South Africa plateau (Baby et al., 2018). In response to domal uplift, major rivers are predicted to deeply incise the planar surfaces and form the present-day south African relief (Roberts and White, 2010). However, to be consistent with regional thermochronological data, the total thickness of regional denudation must be < 1–1.5 km (Wildman et al., 2015; Stanley et al., 2013).

The final cooling event inferred in the thermal history starting at c. 35 Ma and continuing to the present day, is coincident with the timing of the Oligocene unconformity and surface uplift. The thermal history does not show any additional structure that could be correlated with the minor Miocene (c. 11 Ma) unconformity described by Baby et al. (2018). This unconformity is suggested to be traceable across the entire SW African margin and is associated with a dramatic decrease in continental siliciclastic supply (Baby et al., 2018). The thermal impact this event may simply have been too small to be recorded in the data as the samples had already been exhumed to shallower crustal depths and lower temperatures. The cooling history from c. 35 Ma to present-day could be interpreted as a final phase of continuous denudation, which removed a thickness of about 800 m. While the observed unconformities may imply some post-Oligocene erosion, our thermal history would imply sub-aerial erosion in the basin right up to the present-day, which is not the case. Moreover, the offshore record in the Walvis and Orange Basins during the Cenozoic is characterised by low sediment volumes and limited deposition of siliciclastic material from the onshore (Fig. 10) (Baby et al. 2020) and regional onshore erosion rates across Namibia and southwestern African during the Cenozoic, revealed by AFT, AHe and cosmogenic nuclide data, are typically <40 m/Myr (Cockburn et al., 2000; Bierman and Caffee, 2001; Margirier et al., 2019). This is attributed to the prevailing arid climate (Pickford and Senut, 1999) and overall stability of the plateau and relatively small amounts of Oligocene uplift (Baby et al. 2018).

The onset of aridification in the mid-Late Miocene (Pickford and Senut, 1999, Pickford et al., 2014), initiation of the northward flowing cold Benguela current in the Early Oligocene or earlier, leading to the formation of the Namib Desert (van Zinderen Bakker, 1975) and global drop in ocean temperatures of c. 10-15°C from the mid-Eocene Climatic Optimum (~40 Ma)

611 to Present (Zachos et al., 2008) may have all contributed to the final cooling phase, with
612 relatively little denudation required (Fig. 9f). It is possible that the AFT data simply do not
613 have the sensitivity to identify specific thermal perturbations related to the minor Miocene
614 erosion event and/or ocean temperature and the inferred thermal history from 35 Ma to present-
615 day represents a simplified approximation of the most recent cooling experienced by the
616 samples.

617 **CONCLUSIONS**

618 We have presented a suite of AFT data, acquired using both the EDM and LA-ICP-MS
619 methods, on 13 samples from a borehole from offshore Namibia. These data imply the samples
620 have not been hot enough post-deposition to remove all pre-deposition, or inherited, fission
621 tracks. Using Bayesian mixture modelling, we identified AFT age components in each sample,
622 and assigned the AFT data to their most probable age component to produce subsamples. We
623 then obtained detailed thermal history information using a multi-sample inversion approach,
624 using these subsamples. From the pre-depositional part of the thermal history we estimated a
625 distribution of effective AFT closure times for each subsample, and these were generally
626 considerably older than the stratigraphic ages.

627 This novel modelling approach allowed us to recover a record of onshore erosion and offshore
628 sedimentation from a single borehole profile. We identify rapid onshore exhumation at the time
629 of rifting and during the mid-Cretaceous, which is not observed in the onshore Namibian AFT
630 data due to the current level of rock exposure. We also identify a major heating and cooling
631 episode in the late Cretaceous followed be minor heating and cooling of the profile during the
632 Cenozoic. The post-rift events are attributed to regional tectonic and mantle processes,
633 however, the thermal history through the Cenozoic may reflect climate and ocean temperature
634 changes. By combining our LA-ICP-MS fission track data and thermal history paths with REE
635 composition and U-Pb data we make inferences regarding the variations in the sediment
636 sources and reveal mid-late Cretaceous post-rift tectonics drove erosion several 100 kms
637 inland. We have shown how the LA-ICP-MS fission track approach has great future potential
638 in detrital studies by enabling users to acquire an AFT age, FT length information,
639 compositional data and a U-Pb age from a single grain and resolve that grain's thermal history.

640 The inverse thermal history modelling approach was formulated to resolve pre- and post-
641 depositional thermal parts of the thermal history. This was possible because the magnitude of
642 the post-depositional heating was not sufficient to erase provenance related thermal history

643 signals. Clearly there will be many cases where this is not the case, but then higher temperature
644 sensitivity thermochronometers (ZFT, ZHe) may be of use. Thermochronometers sensitive to
645 lower temperatures (AHe, $^{4}He/^{3}He$) would also better constrain the more recent cooling history
646 if all factors causing age dispersion are constrained. Taken together, appropriately selected
647 offshore and onshore thermochronometric datasets should then provide a more integrated and
648 comprehensive source-to-sink evolution model for passive margins.

649

650 **ACKNOWLEDGEMENTS**

651 We would like to thank Canadian Natural Resources Ltd. for granting permission to publish
652 the data. We would also like to thank Nathan Cogné for his comments on an earlier version of
653 this work. This project has received funding from the European Union's Horizon 2020 research
654 and innovation programme under the Marie Skłodowska-Curie grant agreement No. 706976.

655

656 **DATA AVAILABILITY STATEMENT**

657 Data available in article supplementary material

REFERENCES

Amidon, W. H., Roden-Tice, M., Anderson, A. J., McKeon, R. E., & Shuster, D. L. (2016). Late Cretaceous unroofing of the White Mountains, New Hampshire, USA: An episode of passive margin rejuvenation?. Geology, 44(6), 415-418.

Baby, G., Guillocheau, F., Braun, J., Robin, C., & Dall'Asta, M. (2020). Solid sedimentation rates history of the Southern African continental margins: Implications for the uplift history of the South African Plateau. Terra Nova, 32(1), 53-65.

Baby, G., Guillocheau, F., Morin, J., Ressouche, J., Robin, C., Broucke, O., & Dall'Asta, M. (2018). Post-rift stratigraphic evolution of the Atlantic margin of Namibia and South Africa: Implications for the vertical movements of the margin and the uplift history of the South African Plateau. Marine and Petroleum Geology, 97, 169-191.

Barbarand, J., Carter, A., Wood, I., & Hurford, T. (2003). Compositional and structural control of fission-track annealing in apatite. Chemical Geology, 198(1-2), 107-137.

Bernet, M. (2009). A field-based estimate of the zircon fission-track closure temperature. Chemical Geology, 259(3-4), 181-189.

Bernet, M., & Garver, J. I. (2005). Fission-track analysis of detrital zircon. Reviews in Mineralogy and Geochemistry, 58(1), 205-237.

Bierman, P. R., & Caffee, M. (2001). Slow rates of rock surface erosion and sediment production across the Namib Desert and escarpment, southern Africa. American Journal of Science, 301(4-5), 326-358.

Braun, J., Guillocheau, F., Robin, C., Baby, G., & Jelsma, H. (2014). Rapid erosion of the Southern African Plateau as it climbs over a mantle superswell. Journal of Geophysical Research: Solid Earth, 119(7), 6093-6112.

Brown, R. W., Summerfield, M. A., & Gleadow, A. J. (2002). Denudational history along a transect across the Drakensberg Escarpment of southern Africa derived from apatite fission track thermochronology. Journal of Geophysical Research: Solid Earth, 107(B12), ETG-10.

Brown, R., Summerfield, M., Gleadow, A., Gallagher, K., Carter, A., Beucher, R., & Wildman, M. (2014). Intracontinental deformation in southern Africa during the Late Cretaceous. Journal of African Earth Sciences, 100, 20-41.

Carter, A. & Gallagher, K. 2004. Characterising the significance of provenance on the inference of thermal history models from apatite fission track data – A synthetic data study. In: Detrital thermochronology – Provenance analysis, exhumation, and landscape evolution of mountain belts. (Editors: Bernet, M. & Spiegel, C.). GSA Special Paper 378, 7-23.

Cherniak, D. J., & Watson, E. B. (2001). Pb diffusion in zircon. Chemical Geology, 172(1-2), 5-24.

Chew, D. M., & Donelick, R. A. (2012). Combined apatite fission track and U-Pb dating by LA-ICP-MS and its application in apatite provenance analysis. Quantitative Mineralogy and Microanalysis of Sediments and Sedimentary Rocks: Mineralogical Association of Canada, Short Course, 42, 219-247.

Chew, D. M., Donelick, R. A., Donelick, M. B., Kamber, B. S., & Stock, M. J. (2014a). Apatite chlorine concentration measurements by LA-ICP-MS. Geostandards and Geoanalytical Research, 38(1), 23-35.

Chew, D.M., Petrus, J.A. & Kamber, B.S. (2014b). U–Pb LA-ICPMS dating using accessory mineral standards with variable common Pb. Chemical Geology, 363, 185–199.

Clemson, J., Cartwright, J., & Booth, J. (1997). Structural segmentation and the influence of basement structure on the Namibian passive margin. Journal of the Geological Society, 154(3), 477-482.

Clemson, J., Cartwright, J., & Swart, R. (1999). The Namib Rift: a rift system of possible Karoo age, offshore Namibia. Geological Society, London, Special Publications, 153(1), 381-402.

Clift, P. D., Carter, A., & Hurford, A. J. (1996). Constraints on the evolution of the East Greenland Margin: Evidence from detrital apatite in offshore sediments. Geology, 24(11), 1013-1016.

Cockburn, H. A. P., Brown, R. W., Summerfield, M. A., & Seidl, M. A. (2000). Quantifying passive margin denudation and landscape development using a combined fission-track thermochronology and cosmogenic isotope analysis approach. Earth and Planetary Science Letters, 179(3-4), 429-435.

Cogné, N., Chew, D. M., Donelick, R. A., & Ansberque, C. (2020). LA-ICP-MS apatite fission track dating: A practical zeta-based approach. Chemical Geology, 531, 119302.

Cogné, N., Gallagher, K., & Cobbold, P. R. (2011). Post-rift reactivation of the onshore margin of southeast Brazil: evidence from apatite (U–Th)/He and fission-track data. Earth and Planetary Science Letters, 309(1-2), 118-130.

Corner, B. (2000). Crustal framework of Namibia derived from magnetic and gravity data. Communications of the Geological Survey of Namibia, 12, 13-19.

Crowley, K.D. (1993), LENMODEL: A forward model for calculating length distributions and fission-track ages in apatite, Comp. Geosci. 19, 619-626

Dauteuil, O., Bessin, P., & Guillocheau, F. (2015). Cenozoic growth of the southern Africa landscape around the Orange Valley: a planation record of deformation and climate changes. Geomorphology, 233, 5-19.

De Vera, J., Granado, P., & McClay, K. (2010). Structural evolution of the Orange Basin gravity-driven system, offshore Namibia. Marine and Petroleum Geology, 27(1), 223-237.

Frimmel, H. E. (1995). Metamorphic evolution of the Gariep Belt. South African Journal of Geology, 98(2), 176-190.

Gallagher, K. (2012). Transdimensional inverse thermal history modeling for quantitative thermochronology. Journal of Geophysical Research: Solid Earth, 117(B2).

Gallagher, K., & Brown, R. (1997). The onshore record of passive margin evolution. Journal of the Geological Society, 154(3), 451-457.

Gallagher, K., & Brown, R. (1999). Denudation and uplift at passive margins: the record on the Atlantic Margin of southern Africa. Philosophical Transactions of the Royal Society of London. Series A: Mathematical, Physical and Engineering Sciences, 357(1753), 835-859.

Gallagher, K., Brown, R., & Johnson, C. (1998). Fission track analysis and its applications to geological problems. Annual Review of Earth and Planetary Sciences, 26(1), 519-572.

Gallagher, K., Stephenson, J., Brown, R., Holmes, C., & Fitzgerald, P. (2005). Low temperature thermochronology and modeling strategies for multiple samples 1: Vertical profiles. Earth and Planetary Science Letters, 237(1-2), 193-208.

Gibson, S. A., Thompson, R. N., & Day, J. A. (2006). Timescales and mechanisms of plume–lithosphere interactions: 40Ar/39Ar geochronology and geochemistry of alkaline igneous rocks from the Paraná–Etendeka large igneous province. Earth and Planetary Science Letters, 251(1-2), 1-17.

Gilchrist, A. R., & Summerfield, M. A. (1990). Differential denudation and flexural isostasy in formation of rifted-margin upwarps. Nature, 346(6286), 739-742.

Green, P. F., Duddy, I. R., Japsen, P., Bonow, J. M., & Malan, J. A. (2017). Post-breakup burial and exhumation of the southern margin of Africa. Basin Research, 29(1), 96-127.

Guillocheau, F., Rouby, D., Robin, C., Helm, C., Rolland, N., De Veslud, C. L. C., & Braun, J. (2012). Quantification and causes of the terrigeneous sediment budget at the scale of a continental margin: a new method applied to the Namibia–South Africa margin. Basin Research, 24(1), 3-30.

Guillocheau, F., Simon, B., Baby, G., Bessin, P., Robin, C., & Dauteuil, O. (2018). Planation surfaces as a record of mantle dynamics: the case example of Africa. Gondwana Research, 53, 82-98.

Helland-Hansen, W., Sømme, T. O., Martinsen, O. J., Lunt, I., & Thurmond, J. (2016). Deciphering Earth's natural hourglasses: perspectives on source-to-sink analysis. Journal of Sedimentary Research, 86(9), 1008-1033.

Hoernle, K., Rohde, J., Hauff, F., Garbe-Schönberg, D., Homrighausen, S., Werner, R., & Morgan, J. P. (2015). How and when plume zonation appeared during the 132 Myr evolution of the Tristan Hotspot. Nature Communications, 6(1), 1-10.

Holtar, E., and A. W. Forsberg, 2000, Postrift development of the Walvis Basin,Namibia: results from the exploration campaign in Quadrant 1911, inM. R.Mello and B. J. Katz, eds., Petroleum systems of South Atlantic margins: AAPGMemoir 73, p. 429–446

Holzförster, F., Stollhofen, H., & Stanistreet, I. G. (1999). Lithostratigraphy and depositional environments in the Waterberg-Erongo area, central Namibia, and correlation with the main Karoo Basin, South Africa. Journal of African Earth Sciences, 29(1), 105-123.

Homke, S., Vergés, J., Van Der Beek, P., Fernàndez, M., Saura, E., Barbero, L., ... & Labrin, E. (2010). Insights in the exhumation history of the NW Zagros from bedrock and detrital apatite fission-track analysis: evidence for a long-lived orogeny. Basin Research, 22(5), 659-680.

Hurford AJ (1986) Cooling and uplift patterns in the Lepontine Alps South Central Switzerland and an age of vertical movement on the Insubric fault line. Contrib Mineral Petrol 92:413–427

Hurford, A. J., & Green, P. F. (1983). The zeta age calibration of fission-track dating. Chemical Geology, 41, 285-317.

Jasra, A., Stephens, D. A., Gallagher, K., & Holmes, C. C. (2006). Bayesian mixture modelling in geochronology via Markov chain Monte Carlo. Mathematical Geology, 38(3), 269-300.

Jung, S., Brandt, S., Bast, R., Scherer, E. E., & Berndt, J. (2019). Metamorphic petrology of a high-T/low-P granulite terrane (Damara belt, Namibia)–Constraints from pseudosection modelling and high-precision Lu–Hf garnet-whole rock dating. Journal of Metamorphic Geology, 37(1), 41-69.

Jung, S., Hauff, F., & Berndt, J. (2020). Generation of a potassic to ultrapotassic alkaline complex in a syn-collisional setting through flat subduction: Constraints on magma sources and processes (Otjimbingwe alkaline complex, Damara orogen, Namibia). Gondwana Research, 82, 267-287.

Ketcham, R. A., Carter, A., Donelick, R. A., Barbarand, J., & Hurford, A. J. (2007). Improved modeling of fission-track annealing in apatite. American Mineralogist, 92(5-6), 799-810.

Kounov, A., Viola, G., De Wit, M., & Andreoli, M. A. G. (2009). Denudation along the Atlantic passive margin: new insights from apatite fission-track analysis on the western coast of South Africa. Geological Society, London, Special Publications, 324(1), 287-306.

Kounov, A., Viola, G., Dunkl, I., & Frimmel, H. E. (2013). Southern African perspectives on the long-term morpho-tectonic evolution of cratonic interiors. Tectonophysics, 601, 177-191.

Krob, F. C., Eldracher, D. P., Glasmacher, U. A., Husch, S., Salomon, E., Hackspacher, P. C., & Titus, N. P. (2020). Late Neoproterozoic-to-recent long-term t–T-evolution of the Kaoko and Damara belts in NW Namibia. International Journal of Earth Sciences, 109(2), 537-567.

Kroner, S., Konopásek, J., Kroner, A., Passchier, C. W., Poller, U., Wingate, M. T. D., & Hofmann, K. H. (2004). U-Pb and Pb-Pb zircon ages for metamorphic rocks in the Kaoko Belt of Northwestern Namibia: A Palaeo-to Mesoproterozoic basement reworked during the Pan-African orogeny. South African Journal of Geology, 107(3), 455-476.

Ksienzyk, A. K., Dunkl, I., Jacobs, J., Fossen, H., & Kohlmann, F. (2014). From orogen to passive margin: constraints from fission track and (U–Th)/He analyses on Mesozoic uplift and fault reactivation in SW Norway. Geological Society, London, Special Publications, 390(1), 679-702.

Lee, J. K., Williams, I. S., & Ellis, D. J. (1997). Pb, U and Th diffusion in natural zircon. Nature, 390(6656), 159-162.

Leturmy, P., Lucazeau, F., & Brigaud, F. (2003). Dynamic interactions between the Gulf of Guinea passive margin and the Congo River drainage basin: 1. Morphology and mass balance. Journal of Geophysical Research: Solid Earth, 108(B8).

Light, M. P. R., Maslanyj, M. P., Greenwood, R. J., & Banks, N. L. (1993). Seismic sequence stratigraphy and tectonics offshore Namibia. Geological Society, London, Special Publications, 71(1), 163-191.

Malusà, M. G., & Fitzgerald, P. G. (Eds.). (2019). Fission-track thermochronology and its application to geology. Springer International Publishing.

Margirier, A., Braun, J., Gautheron, C., Carcaillet, J., Schwartz, S., Jamme, R. P., & Stanley, J. (2019). Climate control on Early Cenozoic denudation of the Namibian margin as deduced from new thermochronological constraints. Earth and Planetary Science Letters, 527, 115779.

Marsh, J. S. (2010). The geochemistry and evolution of Palaeogene phonolites, central Namibia. Lithos, 117(1-4), 149-160.

Miller, R. M. (1979). The Okahandja lineament, a fundamental tectonic boundary in the Damara Orogen of South West Africa/Namibia. South African Journal of Geology, 82(3), 349-362.

Miller, R. M. (1983). The Pan-African Damara Orogen of South West Africa/Namibia. In Evolution of the Damara Orogen of South West Africa/Namibia.

Moore, M. E., Gleadow, A. J., & Lovering, J. F. (1986). Thermal evolution of rifted continental margins: new evidence from fission tracks in basement apatites from southeastern Australia. Earth and Planetary Science Letters, 78(2-3), 255-270.

O'Connor, J. M., Jokat, W., Le Roex, A. P., Class, C., Wijbrans, J. R., Keßling, S., Kuiper, K. F., & Nebel, O. (2012). Hotspot trails in the South Atlantic controlled by plume and plate tectonic processes. Nature Geoscience, 5(10), 735-738.

O'Sullivan, G., Chew, D., Kenny, G., Henrichs, I., & Mulligan, D. (2020). The trace element composition of apatite and its application to detrital provenance studies. Earth-Science Reviews, 201, 103044.

Passchier, C. W., Trouw, R. A. J., Ribeiro, A., & Paciullo, F. V. P. (2002). Tectonic evolution of the southern Kaoko belt, Namibia. Journal of African Earth Sciences, 35(1), 61-75.

Picart, C., Dauteuil, O., Pickford, M., & Owono, F. M. (2020). Cenozoic deformation of the South African plateau, Namibia: Insights from planation surfaces. Geomorphology, 350, 106922.

Pickford, M., & Senut, B. (1999). Geology and palaeobiology of the Namib desert Southwest Africa. Geological Survey of Namibia, Memoir, 18, 155.

Pickford, M., Senut, B., Mocke, H., Mourer-Chauviré, C., Rage, J. C., & Mein, P. (2014). Eocene aridity in southwestern Africa: timing of onset and biological consequences. Transactions of the Royal Society of South Africa, 69(3), 139-144.

Raab, M. J., Brown, R. W., Gallagher, K., Carter, A., & Weber, K. (2002). Late Cretaceous reactivation of major crustal shear zones in northern Namibia: constraints from apatite fission track analysis. Tectonophysics, 349(1-4), 75-92.

Raab, M. J., Brown, R. W., Gallagher, K., Weber, K., & Gleadow, A. J. W. (2005). Denudational and thermal history of the Early Cretaceous Brandberg and Okenyenya igneous complexes on Namibia's Atlantic passive margin. Tectonics, 24(3).

Roberts, G. G., & White, N. (2010). Estimating uplift rate histories from river profiles using African examples. Journal of Geophysical Research: Solid Earth, 115(B2).

Rouby, D., Bonnet, S., Guillocheau, F., Gallagher, K., Robin, C., Biancotto, F., Dauteuil, O. & Braun, J. (2009). Sediment supply to the Orange sedimentary system over the last 150 My: An

evaluation from sedimentation/denudation balance. Marine and Petroleum Geology, 26(6), 782-794.

Salazar-Mora, C. A., Huismans, R. S., Fossen, H., & Egydio-Silva, M. (2018). The Wilson cycle and effects of tectonic structural inheritance on rifted passive margin formation. Tectonics, 37(9), 3085-3101.

Seiler C, Kohn B, Gleadow A (2014) Apatite fission track analysis by LA-ICP-MS: an evaluation of the absolute dating approach. In: 14th International conference on thermochronology, Chamonix, September 2014, pp 11–12

Stanley, J. R., Flowers, R. M., & Bell, D. R. (2013). Kimberlite (U-Th)/He dating links surface erosion with lithospheric heating, thinning, and metasomatism in the southern African Plateau. Geology, 41(12), 1243-1246.

Tankard, A.J., Jackson, M., Eriksson, K.A., Hobday, D.K., Hunter, D.R., and Minter, W.E.L (1982), Crustal Evolution of Southern Africa 3.8 Billion Years of Earth History, Springer-Verlag Berlin Heidelberg, p. 523, ISBN: 978-1-4613-8149-5

Tinker, J., de Wit, M., & Brown, R. (2008a). Linking source and sink: evaluating the balance between onshore erosion and offshore sediment accumulation since Gondwana break-up, South Africa. Tectonophysics, 455(1-4), 94-103.

Tinker, J., de Wit, M., & Brown, R. (2008b). Mesozoic exhumation of the southern Cape, South Africa, quantified using apatite fission track thermochronology. Tectonophysics, 455(1-4), 77-93.

van der Beek, P., Robert, X., Mugnier, J. L., Bernet, M., Huyghe, P., & Labrin, E. (2006). Late Miocene–recent exhumation of the central Himalaya and recycling in the foreland basin assessed by apatite fission-track thermochronology of Siwalik sediments, Nepal. Basin Research, 18(4), 413-434.

van der Beek, P., Summerfield, M. A., Braun, J., Brown, R. W., & Fleming, A. (2002). Modeling postbreakup landscape development and denudational history across the southeast African (Drakensberg Escarpment) margin. Journal of Geophysical Research: Solid Earth, 107(B12), ETG-11.

van Zinderen Bakker, E. M. (1975). The origin and palaeoenvironment of the Namib Desert biome. Journal of Biogeography, 65-73.

Vasconcelos, P. M., & Carmo, I. D. O. (2018). Calibrating denudation chronology through 40Ar/39Ar weathering geochronology. Earth-Science Reviews, 179, 411-435.

Vermeesch, P. (2018). IsoplotR: A free and open toolbox for geochronology. Geoscience Frontiers, 9(5), 1479-1493.

Wanke, H., & Wanke, A. (2007). Lithostratigraphy of the Kalahari Group in northeastern Namibia. Journal of African Earth Sciences, 48(5), 314-328.

Ward, J. D. (1988). Eolian, fluvial and pan (playa) facies of the Tertiary Tsondab Sandstone Formation in the central Namib Desert, Namibia. Sedimentary Geology, 55(1-2), 143-162.

Ward, J. D., & Martin, H. (1987). A terrestrial conglomerate of Cretaceous age-A new record from the Skeleton Coast, Namib Desert. Commun. Geol. Survey South West Africa/Namibia, 3, 57-58.

Whitchurch, A. L., Carter, A., Sinclair, H. D., Duller, R. A., Whittaker, A. C., & Allen, P. A. (2011). Sediment routing system evolution within a diachronously uplifting orogen: Insights from detrital zircon thermochronological analyses from the South-Central Pyrenees. American Journal of Science, 311(5), 442-482.

Wildman, M., Brown, R., Beucher, R., Persano, C., Stuart, F., Gallagher, K., Schwanethal, J., & Carter, A. (2016). The chronology and tectonic style of landscape evolution along the elevated Atlantic continental margin of South Africa resolved by joint apatite fission track and (U-Th-Sm)/He thermochronology. Tectonics, 35(3), 511-545.

Wildman, M., Brown, R., Persano, C., Beucher, R., Stuart, F. M., Mackintosh, V., Gallagher, K., Schwanethal, J., & Carter, A. (2017). Contrasting Mesozoic evolution across the boundary between on and off craton regions of the South African plateau inferred from apatite fission track and (U-Th-Sm)/He thermochronology. Journal of Geophysical Research: Solid Earth, 122(2), 1517-1547.

Wildman, M., Brown, R., Watkins, R., Carter, A., Gleadow, A., & Summerfield, M. (2015). Post break-up tectonic inversion across the southwestern cape of South Africa: New insights from apatite and zircon fission track thermochronometry. Tectonophysics, 654, 30-55.

Will, T. M., & Frimmel, H. E. (2018). Where does a continent prefer to break up? Some lessons from the South Atlantic margins. Gondwana Research, 53, 9-19.

Zachos, J. C., Dickens, G. R., & Zeebe, R. E. (2008). An early Cenozoic perspective on greenhouse warming and carbon-cycle dynamics. Nature, 451(7176), 279-283

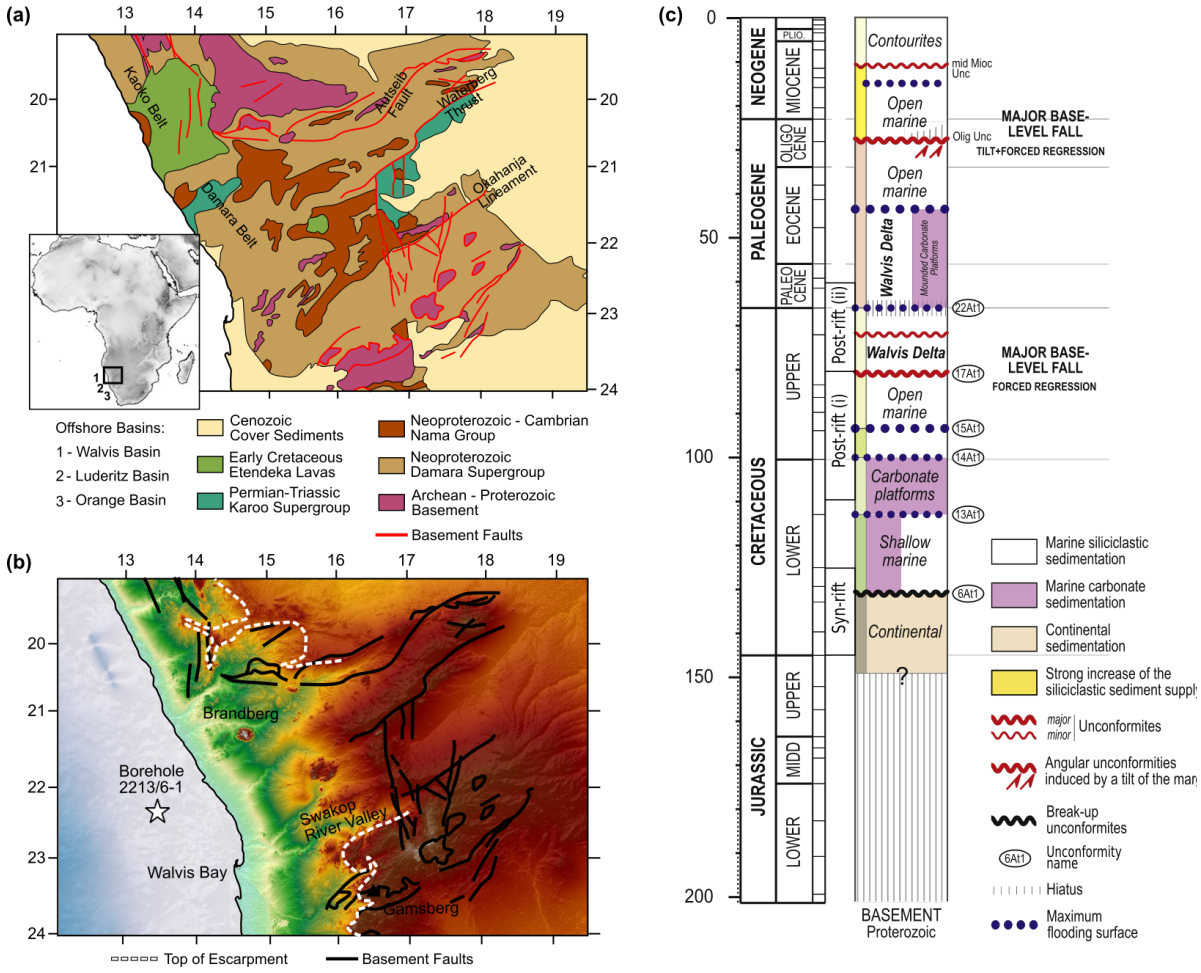

Figure 1: (a) Geological map of north-western Namibia, with inset map of Africa showing the location of the 1 – Walvis, 2 – Lüderitz, and 3 - Orange offshore basins of southwestern Africa, (b) DEM of north-western Namibia showing location of Borehole 2213/6-1, (c) representative stratigraphic column for the Walvis Basin after Baby et al. (2018).

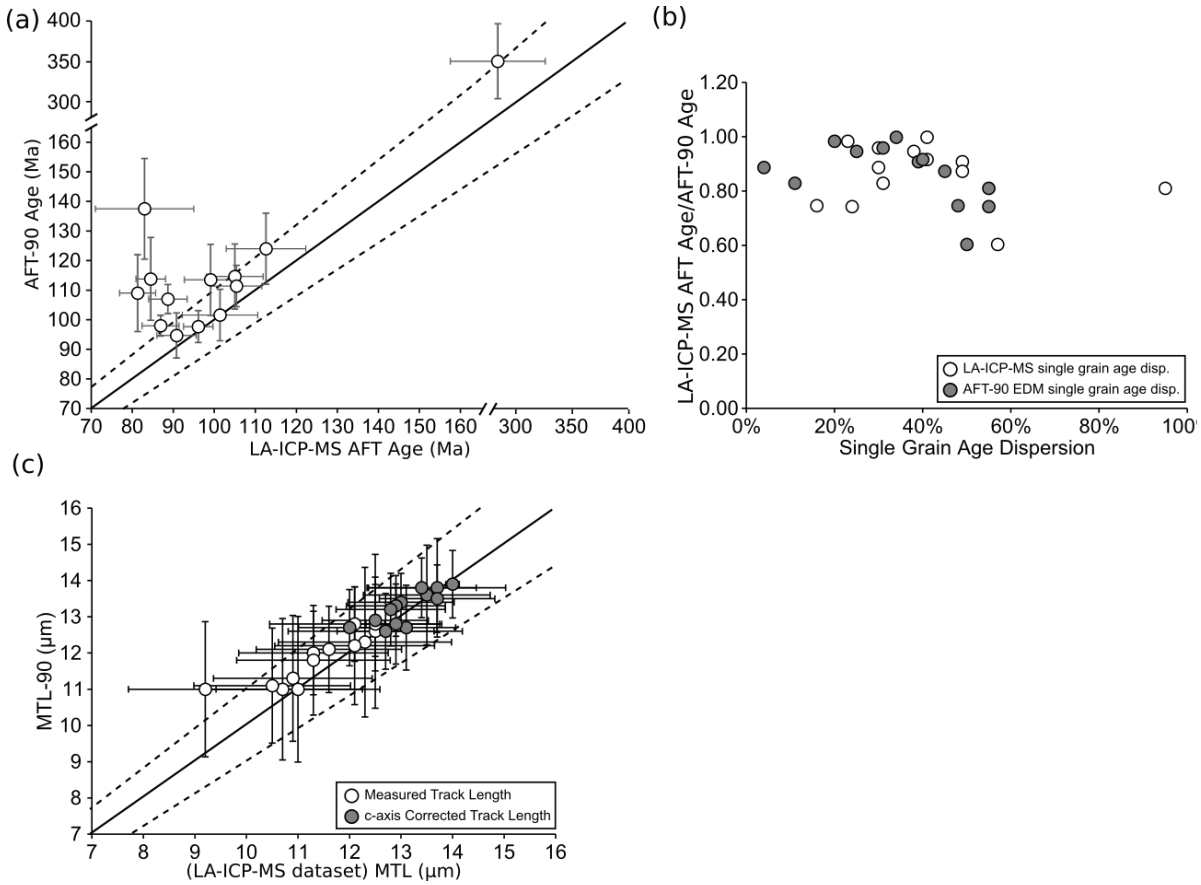

Figure 2: (a) Comparison of central fission track ages for the AFT-90 EDM and LA-ICP-MS datasets; (b) difference between the LA-ICP-MS age and AFT-90 EDM age against the single grain age dispersion for the LA-ICP-MS dataset and AFT-90 EDM dataset (c) comparison of MTLs measured for the AFT-90 dataset and the LA-ICP-MS dataset. Error bars are 1σ s.e. Solid black line represents the 1 to 1 relationship with dashed lines representing ±10%.

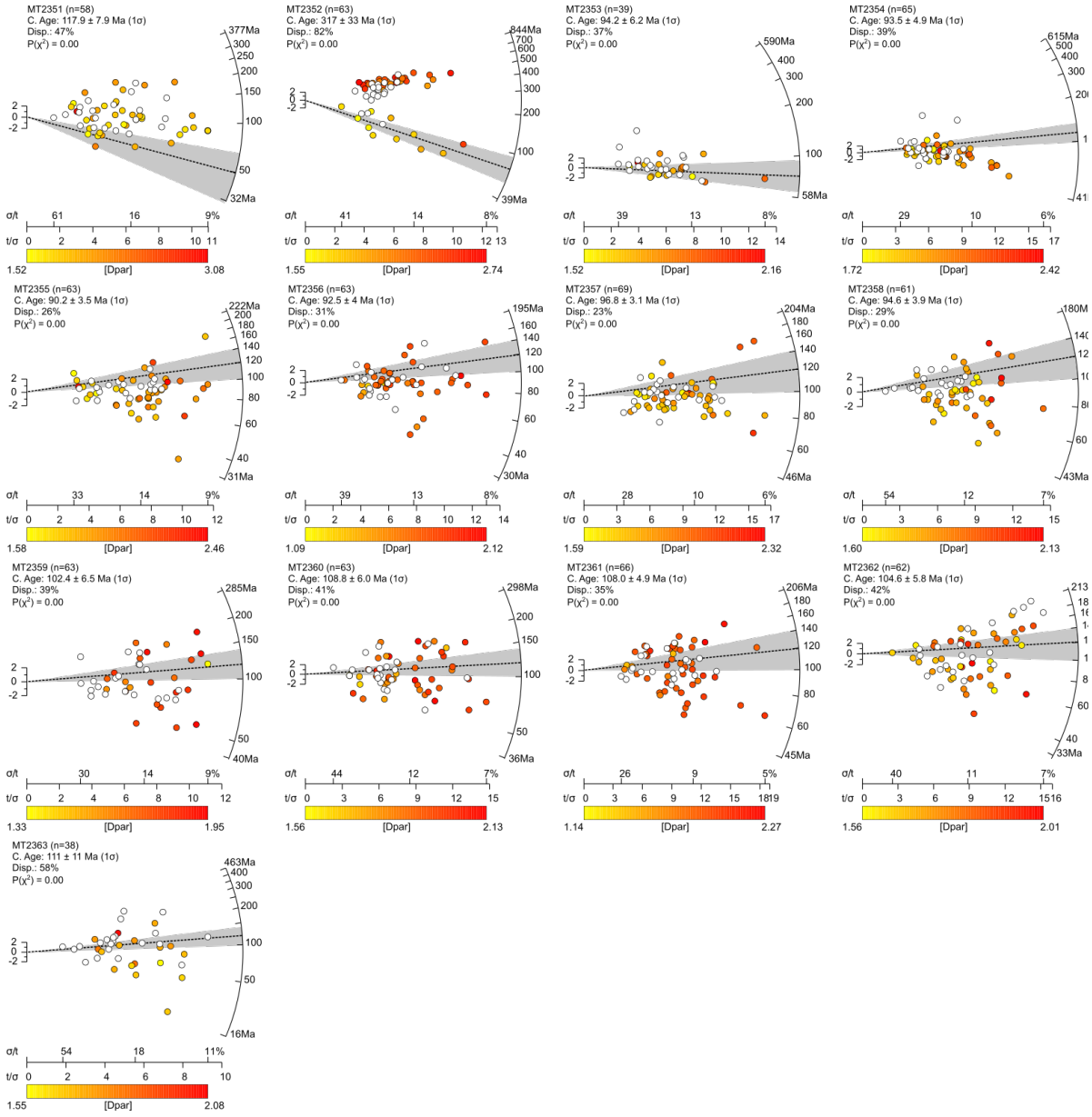

Figure 3: Radial Plots of apatite fission track single grain ages for all samples created using RadialPlotter (Vermeesch, 2018). White circles are data from the AFT-90 dataset and coloured circles from the AFT-2019 dataset. The colour range reflects Dpar size and this range is different for each sample. Note all samples fail the χ^2 statistical test for a homogenous age population (See SI-Table 1 and SI-Table 2 for Chi-Sq values of the AFT-90 and AFT-2019 dataset, respectively). Dashed black line and grey shaded region represents the estimate of the sample stratigraphic age constraint.

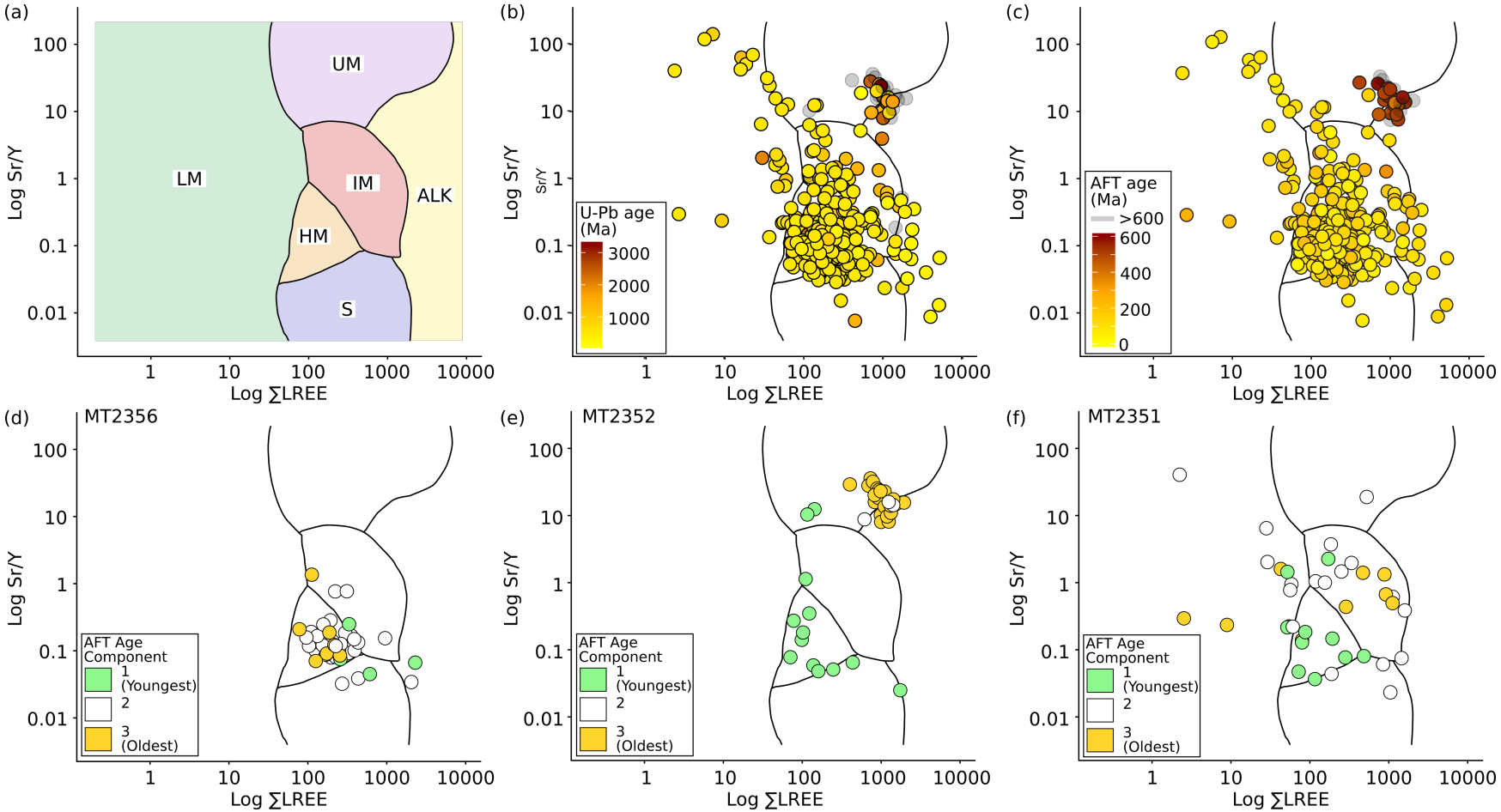

Figure 4: Sr/Y *vs* ΣLREE biplot classification scheme for linking apatite composition to source rock type after O'Sullivan et al. (2020). Abbreviations: ALK = alkali-rich igneous rocks; IM = mafic I-type granitoids and mafic igneous rocks; LM = low- and medium-grade metamorphic and metasomatic; HM = partial-melts/leucosomes/high-grade metamorphic; S = S-type granitoids and high aluminium saturation index (ASI) 'felsic' I-types; UM = ultramafic rocks including carbonatites, lherzolites and pyroxenites. (b) Biplot with data point colour indicating U-Pb age. Grey points represent apatite grains without a U-Pb age. (c) Biplot with data point colour indicating AFT age. Grey points represent apatite grains with AFT age > 600 Ma. (d), (e), and (f) Biplots for individual samples MT2356, MT2352, and MT2351, respectively. Datapoint colour indicates separate AFT age components.

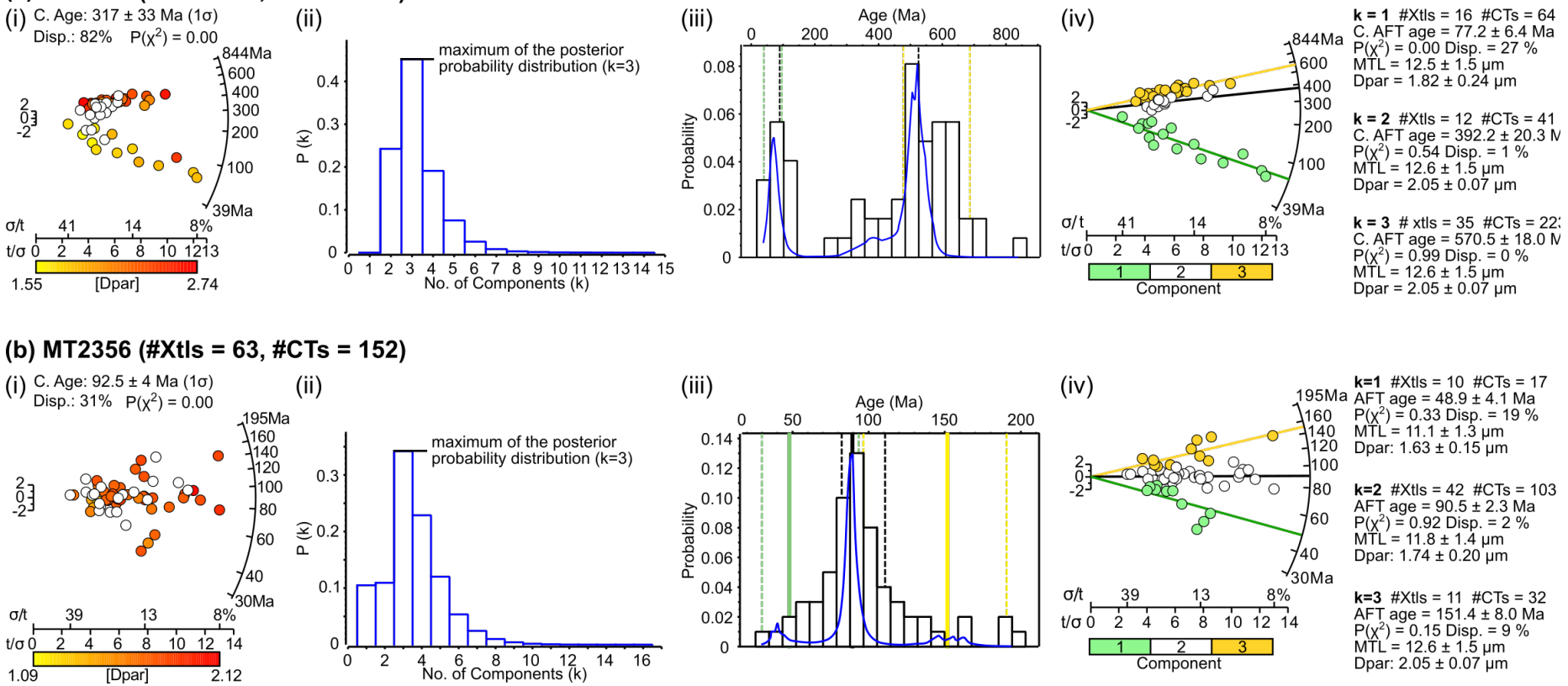

Figure 5: Illustration of obtaining multiple sample components from a single AFT sample dataset for (a) sample MT2352 and (b) sample MT2356. (i) Radial plots of the measured AFT single grain ages (*cf.* Fig. 3), (ii) posterior probability distribution for the inferred number of age components. For both samples it is clear the maximum of the posterior probability distribution is k = 3, (iii) predicted distribution for the maximum posterior 3-component each age model. The solid lines in colour show the mean age for each component, and the dashed lines the 95% credible range about the mean age (iv) allocation of single grain ages (both the AFT-90 and LA-ICP-MS datasets) to a given age component population. The lengths and Dpars were measured on AFT-2019 grains with a measured AFT age and so are also allocated to the same age component as the AFT age for that grain.

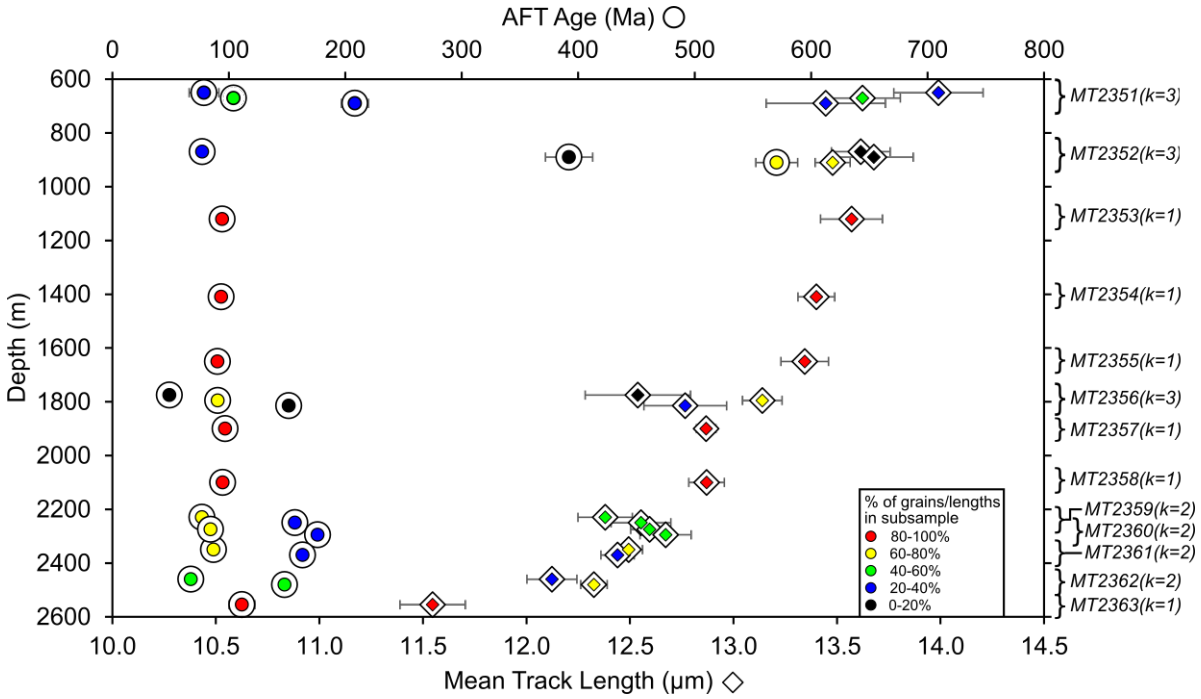

Figure 6: Summary AFT data (13 samples separated into 23 'subsamples'). Note AFT age uncertainty bar is smaller than sample symbol for all but two samples. Open circles represent the central AFT age calculated on each subsample and white diamonds represent mean track length of each subsample (k = estimated number of components). Interior coloured spots represent the proportion of single grain ages and mean track lengths that comprise the subsample. Note that a small vertical offset has been given to subsamples at a particular depth.

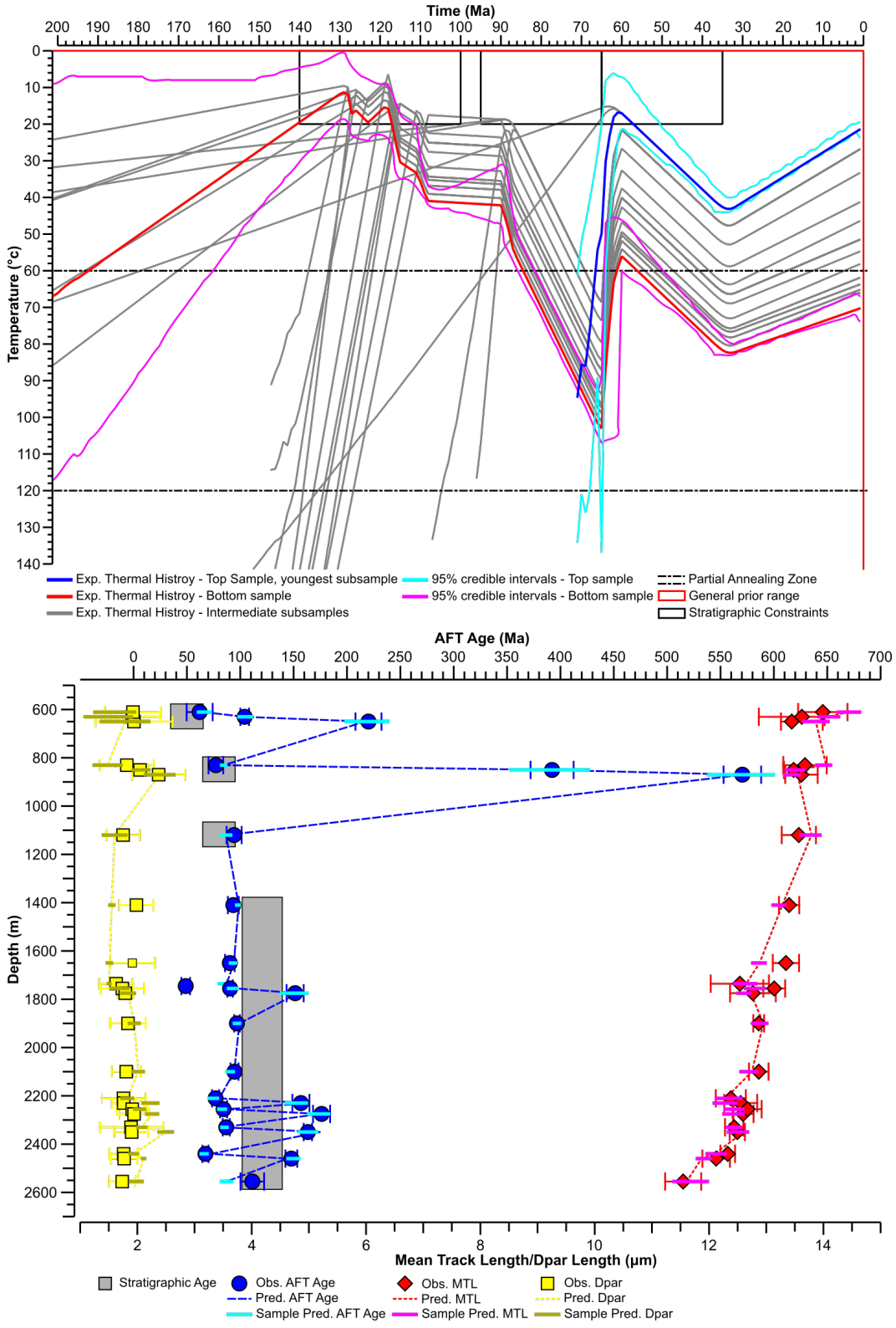

Figure 7: (a) Expected thermal history. Y-axis has been trimmed to 200Ma (see SI-4 for complete thermal history). The blue and red thermal histories (shallowest and deepest samples respectively) also have the 95% credible ranges (cyan and magenta lines). (b) summary of observed and predicted values for AFT age of the 'subsamples' (blue circles = observed, cyan lines = 95% credible range of predictions; mean track length (red diamonds = observed, magenta lines = 95% credible range of predictions) and the sampled values for Dpar (yellow squares and lines = input value, ±1 sigma error range, grey lines, 95% range of resampled values).

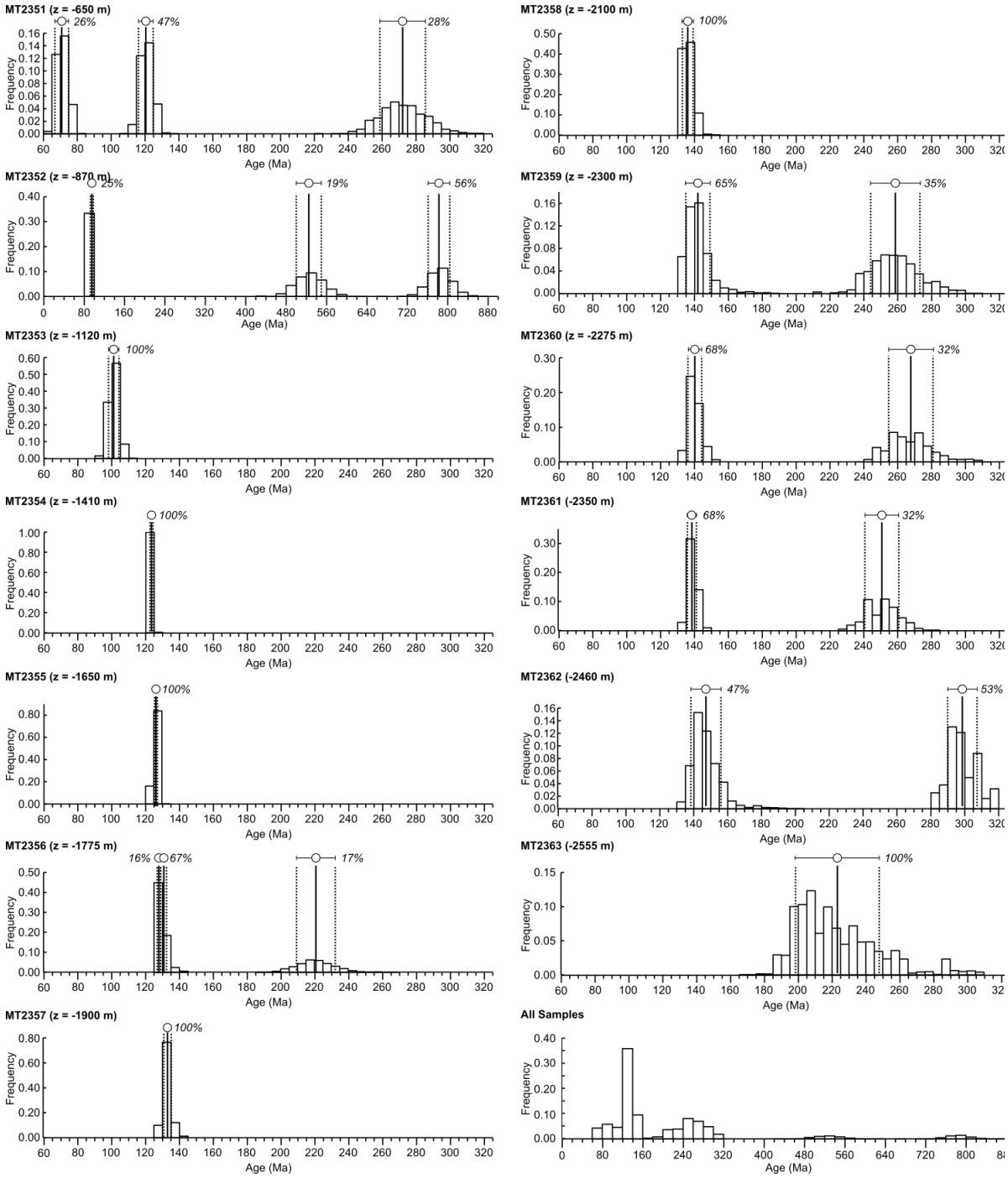

Figure 8: Histograms of estimated apatite fission track closure time, (t_c), from all accepted thermal histories for each of the age components inferred for individual samples. The panel on the bottom right is a summary for all samples. Note the difference in the range of the t_c age scale, on this summary plot and for MT2352 to accommodate the two older components (~540, 800 Ma). Solid lines and white circles represent the age of the mean t_c for each subsample component. Dashed lines and error bars on white circles represent the standard deviation of the mean. Percentage value beside filled circles is the modal abundance of single grains represented by that component.

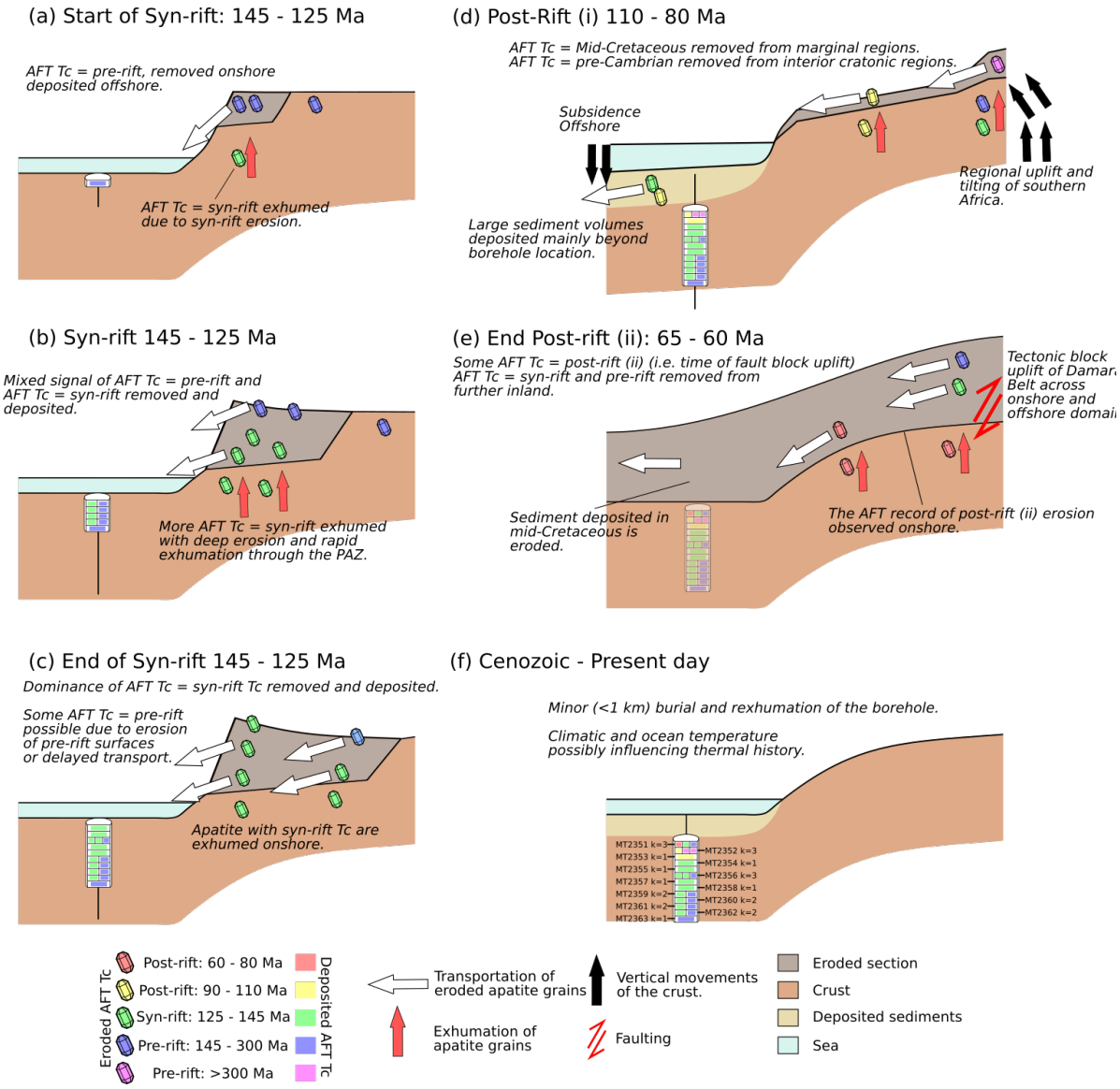

Figure 9: Cartoon showing the exhumation/burial history of the Namibian margin and the removal and deposition of apatite with AFT t_c values reflecting pre-, syn- and post-rift exhumation. (a) Apatite exhumed pre-rift, with pre-rift AFT t_c, are removed at the onset of rifting and deposited first. Apatite with syn-rift t_c are exhumed during syn-rift erosion; (b) Syn-rift erosion produces a mixed signal of pre-rift and syn-rift AFT t_c deposited in the borehole. More apatite with syn-rift t_c are rapidly exhumed through the PAZ due to deep erosion; (c) Dominant syn-rift t_c signal is eroded and deposited. Some older t_c are possible due to erosion of pre-rift surfaces or delayed transport. (d) Regional uplift and tilting of southern Africa. Erosion exhumes and removes apatite with mid-Cretaceous t_c from marginal regions and with pre-Cambrian t_c from interior cratonic regions. With westward tilting, large volumes of sediment are delivered to the basin and mainly deposited in regions beyond borehole location. The borehole is buried until the onset of Late Cretaceous reactivation at c. 65–60 Ma (e) Local block uplift of Damara Belt in onshore and offshore domains. Some apatite, rapidly cooled, with t_c reflecting the time of fault block uplift eroded. Apatite eroded from further inland have older t_c. AFT record of erosion at this time remains onshore. Material that buried the borehole following mid-Cretaceous uplift and tilting is eroded. (f) Cenozoic vertical movements may have led to minor (<1 km) burial and re-exhumation before borehole resided at its present-day setting. Changing climatic and ocean temperature conditions may influence the geotherm and the recent thermal history of the borehole.

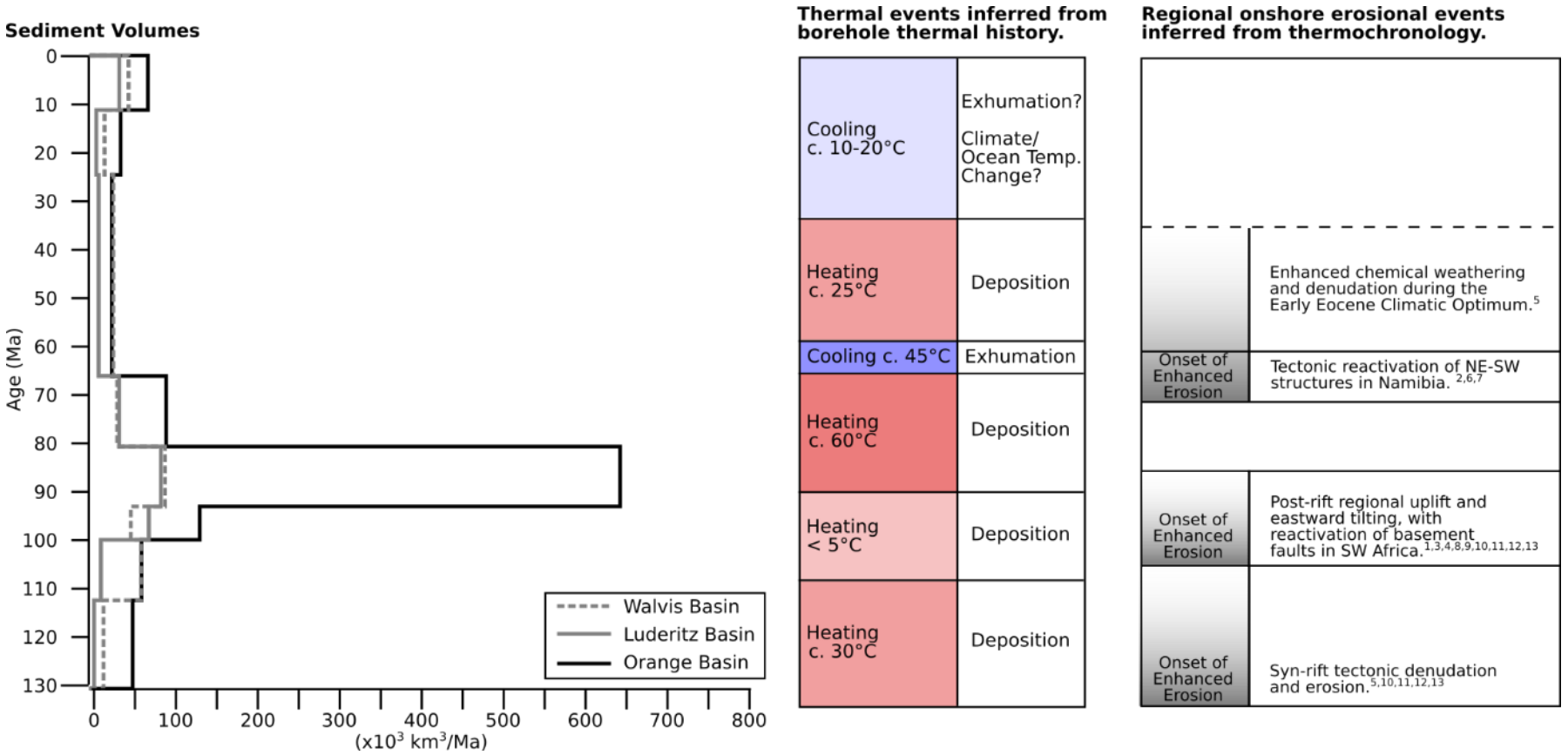

Figure 10: Comparison of sediment accumulation volumes in the Walvis, Lüderitz and Orange basins (after Baby et al., 2020) - the main depocenters for eroded material from Namibia and southwestern Africa – with cooling history of the borehole profile (*cf.* Fig. 7) collected in the Walvis Basin and the timing of major erosional events recorded onshore by low temperature thermochronology studies. References for thermochronology datasets: 1 – Brown et al., 2002, 2- Brown et al., 2014, 3 – Kounov et al., 2009, 4 – Kounov et al., 2013, 5 –Margirier et al., 2019, 6 – Raab et al., 2002, 7 – Raab et al., 2005, 8 – Stanley et al, 2013, 9 – Stanley et al., 2015, 10 – Tinker et al., 2008a, 11 – Wildman et al., 2015, 12 – Wildman et al., 2016, 13 – Wildman et al., 2017.

Sample	Strat. Age	Depth (m)	N_s	N_i^*	$P(\chi^2)$	Disp.	C. AFT Age	#Xtls	MTL	SD	Proj. MTL	SD	#CT	Dpar	SD
MT2351	50 ± 20	650	3325	6464	0.00	47%	117.9 ± 7.9	58	12.56 ± 0.13	1.90	13.74 ± 0.09	1.34	214	1.95 ± 0.02	0.35
MT2352	80 ± 15	870	6727	5472	0.00	82%	317 ± 33	63	12.31 ± 0.09	1.78	13.55 ± 0.06	1.27	430	2.20 ± 0.02	0.41
MT2353	80 ± 15	1120	2111	5224	0.00	37%	94.2 ± 6.2	39	12.70 ± 0.11	1.31	13.82 ± 0.08	0.96	153	1.79 ± 0.02	0.27
MT2354	120 ± 20	1410	5397	13580	0.00	39%	93.5 ± 4.9	65	12.37 ± 0.09	1.48	13.57 ± 0.06	1.00	255	1.99 ± 0.02	0.25
MT2355	120 ± 20	1650	4862	11890	0.00	26%	90.2 ± 3.5	63	12.17 ± 0.11	1.58	13.44 ± 0.07	1.07	207	1.93 ± 0.01	0.28
MT2356	120 ± 20	1775	4592	10882	0.00	31%	92.4 ± 4	63	11.81 ± 0.08	1.35	13.16 ± 0.06	0.96	263	1.75 ± 0.01	0.25
MT2357	120 ± 20	1900	8294	18220	0.00	23%	96.8 ± 3.1	69	11.46 ± 0.06	1.42	12.96 ± 0.04	0.96	515	1.85 ± 0.01	0.25
MT2358	120 ± 20	2100	5472	12851	0.00	29%	94.6 ± 3.9	61	11.48 ± 0.09	1.52	12.96 ± 0.06	1.05	271	1.81 ± 0.01	0.24
MT2359	120 ± 20	2230	3593	7835	0.00	39%	102.4 ± 6.5	43	11.11 ± 0.11	1.65	12.69 ± 0.07	1.04	219	1.77 ± 0.01	0.20
MT2360	120 ± 20	2275	6789	13963	0.00	41%	108.8 ± 6	63	11.05 ± 0.10	1.73	12.66 ± 0.06	1.08	311	1.93 ± 0.01	0.24
MT2361	120 ± 20	2350	9436	20089	0.00	35%	108 ± 4.9	66	10.80 ± 0.08	1.67	12.53 ± 0.05	1.03	459	1.93 ± 0.01	0.25
MT2362	120 ± 20	2460	8980	17808	0.00	42%	104.6 ± 5.8	62	10.66 ± 0.08	1.56	12.37 ± 0.05	1.02	418	1.77 ± 0.01	0.21
MT2363	120 ± 20	2555	1829	4442	0.00	58%	111 ± 11	38	10.45 ± 0.18	1.94	12.29 ± 0.11	1.17	118	1.72 ± 0.01	0.22

Table 1: Summary of AFT data (composite AFT-90 + LA-ICP-MS AFT data. See SI-Table 1 and SI-Table 2 for summary data of AFT-90 and LA-ICP-MS AFT datasets. N_s = Total number of spontaneous tracks. N_i = Total number of induced tracks. *The total number of N_i is the sum of the N_i counted in the AFT-90 EDM dataset and the N_i determined for each grain dated using LA-ICP-MS based on the measured LA-ICP-MS AFT age, its error and the zeta calibration factor, ρ_d and N_d (track density and number of tracks counted for the U dosimeter) from the AFT-90 EDM analyses. $P(\chi^2)$ is the chi-squared test for population homogeneity. Disp. = the single grain age dispersion. C. AFT Age = central AFT age and 1σ standard error. #Xtls = total number of crystals dated (AFT-90 and LA-ICP-MS data combined). MTL = mean track length (measured in the LA-ICP-MS AFT samples only) and 1σ standard error. Proj. MTL = mean track length corrected for c-axis orientation and 1σ standard error. #CT = number of confined track lengths measured in both LA-ICP-MS and AFT-90 EDM datasets. D_{par} = mean etch pit size and 1σ standard error. SD = standard deviation on length measurements.

Group	Pre-depositional cooling		Subsample	Stratigraphic Age
I	Protracted cooling initiated prior to 150 Ma		MT2363-1	120 ± 20 Ma
			MT2362-2	
			MT2361-2	
			MT2360-2	
			MT2359-2	
			MT2356-3	
			MT2352-3	80 ± 15 Ma
			MT2352-2	
			MT2351-3	50 ± 15 Ma
II	Rapid cooling across the base of the Partial Annealing Zone (PAZ) between 145–125 Ma		MT2362-1	120 ± 20 Ma
			MT2361-1	
			MT2360-2	
			MT2359-1	
			MT2358-1	
			MT2357-1	
			MT2356-2	
			MT2356-1	
			MT2355-1	
			MT2354-1	
			MT2351-2	50 ± 15 Ma
III	Rapid Late Cretaceous cooling initiating at:	100 - 90 Ma	MT2353-1	80 ± 15 Ma
			MT2352-1	
		70 Ma	MT2351-1	

Table 2: Summary of pre-depositional thermal history for each subsample. See SI-4 for an illustration of the thermal history split into the three groups.